# Chapter 2
# Theoretical Background

This chapter gives an overview of the two base systems of gelled bicontinuous microemulsions, namely bicontinuous microemulsions (Sect. 2.1) and binary gels (Sect. 2.2). Moreover, the basics of the three techniques which were used extensively for studying the systems' characteristic properties and their microstructure are introduced. Thus Sect. 2.3 deals with rheology, Sect. 2.4 with Fourier transform pulsed-gradient spin-echo NMR spectroscopy and Sect. 2.5 with small angle neutron scattering.

## 2.1 Base System 1: Bicontinuous Microemulsion

Quite intuitively, the first base system of a gelled bicontinuous microemulsion is the respective non-gelled, low viscous bicontinuous microemulsion without any gelator. Nevertheless, the system contains at least three components, namely a polar, a non-polar and an amphiphilic one. These are self-assembled in a way that the polar and the non-polar component form continuous, interpenetrating domains which are separated by a monolayer of the amphiphile. In fact, this is why one calls the system 'bicontinuous'. One distinguishes bicontinuous microemulsions from so-called 'droplet microemulsions' in which discrete droplets of the polar component are dispersed in a continuous non-polar phase or vice versa. The characteristic features of all microemulsions are that their microstructure is nanometer-sized and that they are formed via spontaneous self-assembly, which is why they are thermodynamically stable [1]. The name 'microemulsion' is thus counterintuitive, however, it dates back to times when these interesting systems were far from being understood. Schulman and Winsor initiated the research on microemulsions when they described the systems' composition and exceptional properties, such as their transparency and ultra-low interfacial tension, in 1943 and 1954, respectively [2, 3]. In the following Friberg, Shinoda and their co-workers investigated the phase behaviour of microemulsions [4–6], on which further extensive studies were carried out by Kahlweit and Strey [7–10]. It turned out that close relations exist between the systems' properties, microstructure and phase

behaviour [11]. Up to today an in-depth knowledge has been acquired in the field, particularly about "simple" microemulsions like, e.g., ternary systems consisting of water, $n$-alkane and a non-ionic surfactant. Thus scientists are now exploring various fields of applications for microemulsions, including their use as reaction media [12], templating materials [13], detergents [14], drug delivery systems [15] and much more. This of course requires an understanding of the complex interplay of the classical microemulsion system with the components which are added for the specific application. The work at hand contributes a piece to this understanding by investigating the mutual effects of a bicontinuous microemulsion and an added gelator. This combination could, for example, be interesting for gelled micro-emulsion skin care formulations which would be easy to administer and feature enhanced residence times of the active ingredients.

## 2.1.1  Composition of Microemulsions

As mentioned before, microemulsions are liquid systems comprising at least three components two of which are intrinsically immiscible due to different polarity and a third one which mediates between the first two such that macroscopically homogeneous mixtures are formed. The polar component in a microemulsion is usually **water**, just as it is the case in this thesis. In principle it is of course also possible to employ other polar substances such as formamide [16] or ionic liquids [17]. However, rather than that one finds microemulsions comprising aqueous solutions of salts [9] or other polar additives. The second, non-polar component is commonly referred to as '**oil**'. It is often an aromatic or aliphatic (cyclic or non-cyclic) hydrocarbon but also vegetable oils (e.g. soybean oil [18]) or other non-polar substances, like supercritical $CO_2$ [19], are used. If people work with mixtures of different oils they call the minor component the 'co-oil'. In the work at hand the used oil is $n$-decane, i.e. a linear hydrocarbon with a boiling point of 174 °C and a density of 0.730 g cm$^{-3}$ [20]. When it comes to the **amphiphile** the variety of possible substances is even more extended than is the case for the oil component. One usually classifies surface active compounds on the basis of their polar 'head group' which is bound to a non-polar moiety, usually a long hydro-carbon chain. One distinguishes ionic from non-ionic surfactants whose head groups are charged and non-charged, respectively. Moreover one can specify the chemical structure of the head group, which can, e.g., be a carbohydrate as it is the case in 'sugar surfactants' or a polyethylene glycol unit like in the here used tetraethylene glycol monodecyl ether ($C_{10}E_4$). The latter is from the group of the non-ionic '$C_iE_j$ surfactants' which possess $j$ ethylene glycol units in their head group and an $n$-alkyl chain with $i$ carbon atoms. $C_iE_j$ surfactants have been used, together with water and $n$-alkanes, for comprehensive and systematic studies of the phase behaviour and properties of microemulsions, e.g. [8, 10, 21]. These systems

are convenient for this purpose because they form microemulsions without 'co-surfactants' which are needed with many other mixtures. The possibility to work with a minimum number of simple substances is always advantageous for systematic studies, hence also in the thesis at hand. This explains the choice of the used microemulsion components water, $n$-decane and $C_{10}E_4$ and also the decision to work with a pure instead of a much cheaper technical-grade surfactant, which constitutes a mixture of amphiphiles whose head groups and chain lengths possess a certain distribution.

According to the conventional nomenclature one simply lists the polar, the non-polar and the amphiphilic component separated by dashes to name a microemulsion and separates additives by a slash from the respective main component, i.e. water/polar additive–oil/co-oil–surfactant/co-surfactant. Hence the here described base microemulsion is $H_2O$–$n$-decane–$C_{10}E_4$ while the gelled microemulsion is $H_2O$–$n$-decane/12-HOA–$C_{10}E_4$, where 12-HOA is denoted as "co-oil" because it is an organogelator notwithstanding the claimed coexistence of the gelator network with the entire microemulsion.

To specify the quantitative composition of a microemulsion several variables are introduced. First, one states the ratio of water to oil either as mass fraction

$$\alpha = \frac{m_{\text{oil}}}{m_{\text{water}} + m_{\text{oil}}} \tag{2.1}$$

or as volume fraction

$$\phi = \frac{V_{\text{oil}}}{V_{\text{water}} + V_{\text{oil}}} \tag{2.2}$$

where $m$ and $V$ are the masses and volumes of the components, respectively. For reasons which will be explained below all microemulsions in this work were prepared with equal volumes of water and $n$-decane, thus $\phi = 0.5$ which corresponds to $\alpha = 0.422$. Secondly, the surfactant concentration is quoted, generally as its mass fraction in the total mixture and thus here as

$$\gamma = \frac{m_{\text{surfactant}}}{m_{\text{water}} + m_{\text{oil}} + m_{\text{surfactant}} + m_{\text{gelator}}}. \tag{2.3}$$

The concentration of the gelator is defined in this thesis by

$$\eta = \frac{m_{\text{gelator}}}{m_{\text{water}} + m_{\text{oil}} + m_{\text{surfactant}} + m_{\text{gelator}}}, \tag{2.4}$$

which is the last parameter needed to fully quantify the composition of a $H_2O$–$n$-decane/12-HOA–$C_{10}E_4$ microemulsion.

## 2.1.2 Phase Behaviour

When water, oil and a surfactant are mixed it depends on the composition of the mixture whether a microemulsion is formed or not. Moreover, one often finds the microemulsion coexisting with a water or/and an oil excess phase in a macro-scopically two-phase or three-phase system, respectively [1]. Which situation is encountered can be read from a 'phase diagram' of the system. Given that the system comprises three different components, a suitable phase diagram is a Gibbs triangle the three corners of which stand for water, oil and the surfactant, respectively. However, since the formation of a microemulsion often also depends on additional parameters, like the concentration of a co-surfactant or the tem-perature, most phase diagrams need to be expanded in a third dimension. In the case of the here discussed ternary water–*n*-alkane–non-ionic surfactant micro-emulsions the temperature-dependent phase behaviour is fully mapped by a phase prism [22] like the one schematically shown in Fig. 2.1. It can be seen as a stack of isothermal Gibbs triangles as the ordinate axis represents the temperature. The three vertical sides of the prism are the temperature-composition phase diagrams of the binary systems water–oil, water–surfactant and oil–surfactant, respectively. The interplay of their miscibility gaps determines the location of the multi-phase regions within the phase prism. Accordingly, one can also imagine that the prism results from "folding" the three binary phase diagrams together.

To understand the quite complex phase prism it is reasonable to first "unfold" it and look at the binary phase diagrams separately (see Fig. 2.2). The water–oil mixture possesses, as expected, a large miscibility gap which expands for all accessible temperatures over nearly the whole composition range. Water and surfactant, by contrast, mix at low temperatures but with increasing temperature one runs into a (closed) upper miscibility gap with a lower critical point $cp_\beta$ at a critical temperature $T_\beta$, which is usually between 0 and 100 °C. Note that for long-chain surfactants the water–surfactant phase behaviour is much more complex since one also finds liquid crystalline regions; however, this is neglected in the simple representation of Fig. 2.2. The third binary system, oil–surfactant, possess a critical point $cp_\alpha$ which belongs to a lower miscibility gap. The corresponding upper critical temperature $T_\alpha$ normally lies around or somewhat below 0 °C. In a nutshell, the descriptions of the binary systems reveal that the water solubility of the surfactant decreases with increasing temperature while its solubility in oil increases.

The isothermal Gibbs triangles certainly reflect the described behaviour as well (cp. Fig. 2.1). They show at high temperatures two-phase regions with tie-lines sloped in the direction of the water corner indicating the coexistence of a sur-factant-rich oil phase with a water excess phase. At low temperatures the situation is inversed and one finds a surfactant-rich water phase coexisting with an excess oil phase. Note that the temperature-dependence of the surfactant's head group hydration, which is high at low and low at high temperatures, essentially influences the described behaviour in the three component mixture because the most part of
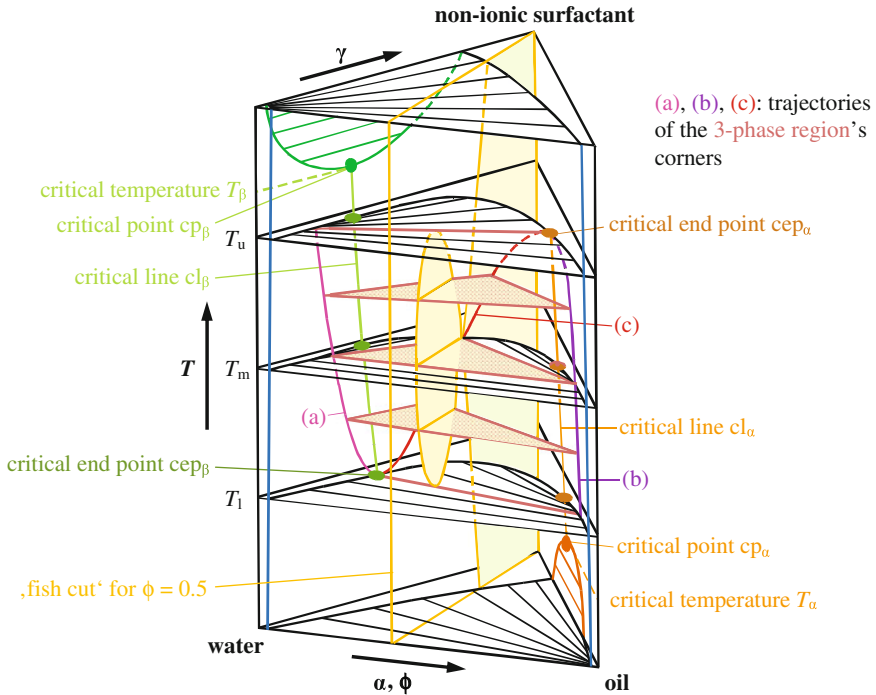
**Fig. 2.1** Schematic phase prism describing the temperature-dependence of a ternary water–oil–non-ionic surfactant microemulsion system (adapted from [89] with permission of the Bunsen Society)

**Fig. 2.2** Unfolded phase prism showing the miscibility gaps in the temperature-composition phase diagrams of the binary systems (adapted from [10] with permission of John Wiley and Sons)
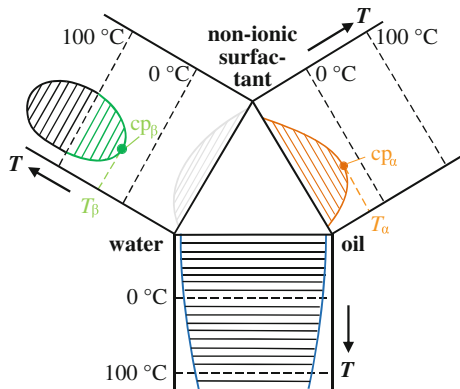


the surfactant is not dissolved in the oil or the water bulk phase as will be explained below. In any case, the gradual inversion from a surfactant-rich water phase at low to a surfactant-rich oil phase at high temperatures results in the formation of a distinct surfactant phase at intermediate temperatures. The latter

coexists with both an oil and a water excess phase in a temperature range between $T_l$ ("$T$ lower") and $T_u$ ("$T$ upper") where a three-phase region is formed. The temperature in the middle of the three-phase range, i.e. the mean temperature $T_m = (T_l + T_u)/2$, is called the 'phase inversion temperature' (PIT). Interestingly, it is exactly at $T_m$ where a minimum amount of surfactant is needed to form a one-phase ternary mixture with equal volumes of water and oil. This follows from geometrical considerations taking into account different trajectories in the phase prism such as the critical lines $cl_\alpha$ and $cl_\beta$ (cp. Fig. 2.1).

Since the three-dimensional phase prism is pretty complex it is hardly possible to fully determine it for every microemulsion system under investigation. Hence one usually limits oneself to studying a "cut" through the prism, like for example an isothermal Gibbs triangle for a certain temperature. This is often sufficient to extract the required information about the system. The cut which was used throughout this work is a $T$-$\gamma$ cut for which the temperature and the surfactant concentration are varied while the water-to-oil ratio is held constant. With the equal volumes of water and oil that were used the $T$-$\gamma$ diagram possesses phase boundaries which are in the ideal case symmetric with respect to the $T_m$ temperature. Furthermore they resemble the contour of a schematic fish such that one also speaks of a 'fish cut diagram' (see Figs. 2.1 and 2.3). On the left hand side of the $T$-$\gamma$ diagram, i.e. for small surfactant mass fractions $\gamma$, the water–oil–non-ionic surfactant mixture consists of two immiscible phases of water and oil. The comprised surfactant self-assembles at the interfacial area and dissolves in part monomerically in the two bulk phases, in particular in the oil. With increasing $\gamma$ one reaches a surfactant concentration $\gamma_0$ at which the bulk phases are saturated and the water–oil-interface is fully occupied by a surfactant monolayer. Thus beyond $\gamma_0$ the surfactant concentration is high enough to solubilize water and oil into one another, i.e. a microemulsion is formed. According to the explanations given above it depends on the temperature whether oil is solubilized in water or vice versa. In any case the surfactant-rich phase constitutes the microemulsion which coexists with so-called 'excess phases'. While an oil excess phase is present at low and a water excess phase at high temperatures one finds both excess phases coexisting with a newly formed microemulsion phase at medium temperatures. Note that the two-phase regions are named $\underline{2}$ and $\overline{2}$; the dash indicating the location of the microemulsion phase. Since with the addition of surfactant more and more volumes of water and oil can be solubilized into one another the excess phases shrink with increasing $\gamma$ until the water–oil–surfactant mixture is one-phase. The smallest amount of surfactant needed to reach the one-phase region is $\widetilde{\gamma}$, which is therefore referred to as the microemulsion's 'efficiency'. Together with the temperature $\widetilde{T}$, which in an ideal system is just the phase inversion temperature $T_m$, $\widetilde{\gamma}$ determines the so-called $\widetilde{X}$ point which is an important and often stated parameter characterizing the microemulsion system.

**Fig. 2.3** Schematic $T$-$\gamma$ ('fish cut') diagram of a water–oil–non-ionic surfactant microemulsion with test tubes illustrating the different phases
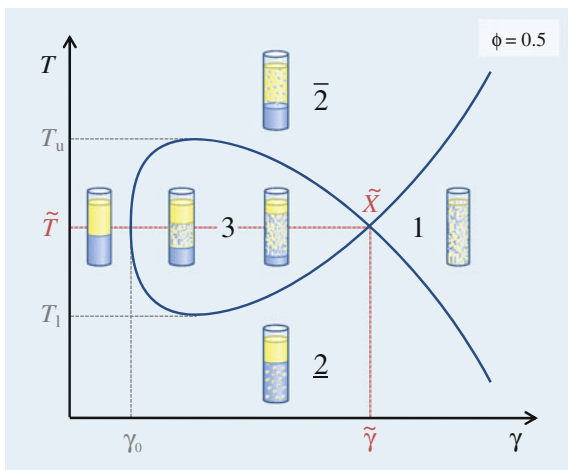


### 2.1.3 Microstructure

Very characteristic for microemulsions is, besides the just discussed phase behaviour, their microstructure which is nanometer-sized [1]. Note that the wavelength of visible light is just somewhat larger than the microstructure which explains why microemulsions often appear transparent and show the Tyndall effect. What type of microstructure is formed depends on the local curvature of the amphiphilic film [23] which is determined by the structure and conformation of the surfactant molecules at the water–oil interface. Depending on whether the surfactant's hydrophilic (and hydrated) head groups or their lipophilic chains are sterically more demanding the surfactant monolayer either bends around the oil or around the water, respectively. To quantify this behaviour one specifies the 'mean curvature' of the surfactant film as

$$H = \frac{c_1 + c_2}{2} \tag{2.5}$$

where $c_1$ and $c_2$ are the film's principal curvatures, i.e. the reciprocal radii $R_1$ and $R_2$ of two orthogonal osculating circles at a certain point on the film (cp. Fig. 2.4, right).

Generally, curvature around oil is defined positive and curvature around water negative. If the surfactant film is in an 'optimal shape' $c_1$ and $c_2$ adopt values for which the Helfrich bending energy per unit film area [24]

$$f = 2\kappa(H - H_0)^2 + \overline{\kappa}\, c_1\, c_2 \tag{2.6}$$

becomes minimal. In this equation $\kappa$ and $\overline{\kappa}$ are elasticity moduli which are measures for the film rigidity and the energy cost to form structures with connected

**Fig. 2.4** Three-dimensional
model of a bicontinuous
structure (*left*, modified from
[90]) and its local saddle-like
conformation (*right*)
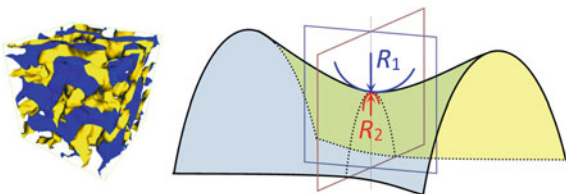


**Fig. 2.5** Schematic
representation of the different
microstructures which occur
in water–oil–non-ionic
surfactant microemulsions as
a function of temperature
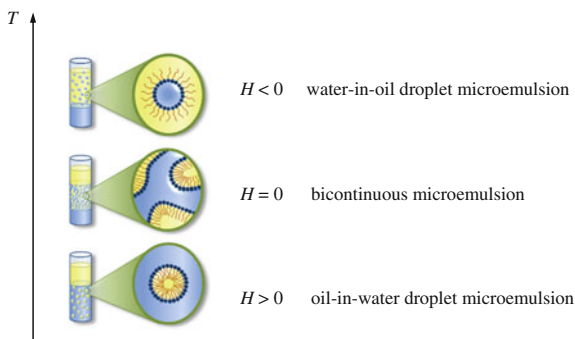


topology (like bicontinuous structures, Fig. 2.4), respectively. $H_0$ is the spontaneous curvature which the interfacial layer would adopt if there were no external
forces, thermal fluctuations or conservation constrains.

Due to the very low interfacial tensions in microemulsions the spontaneous
curvature is usually quite low, i.e. the curvature radius is much bigger than the
thickness of the surfactant layer ($\sim 1$ nm). Therefore the surfactant film is very
flexible and fluctuates permanently. The most flexible surfactant layer with the
strongest fluctuations, along with an ultra-low interfacial tension between the
water and the oil phase (down to about $10^{-4}$ N m$^{-1}$ [25]), is found in bicontinuous
microemulsions. Here water and oil domains interpenetrate such that a "sponge-
like" microstructure with local saddle-like conformations is formed (cp. Fig. 2.4).
Thus the interfacial layer is locally planar and for the mean curvature it holds
$H = 0$. One also speaks of a "balanced" state since the surfactant head group and
chain have effectively the same space requirements. If the latter is not the case the
mean curvature deviates from zero and in the extreme cases spherical droplets of
water or oil are formed. The mean curvature $H$ is then the reciprocal droplet radius
with a positive sign for oil and a negative sign for water droplets. A descriptive
reason for the droplet formation is increased repulsive forces which act between
the head groups or between the alkyl chains of the surfactant, respectively. In the
case of non-ionic surfactants these forces are governed by temperature (cp.
Fig. 2.5). When the temperature is low the surfactant head groups are strongly
solvated and thus bulky. Hence oil droplets are formed which are dispersed in a
continuous   water   phase   ('oil-in-water   droplet   microemulsion').   At   high

temperatures, in contrast, the hydration shell around the head groups is considerably reduced while the alkyl chains are in increased thermal motion. Accordingly one finds a 'water-in-oil (w/o) droplet microemulsion'.

One can conclude that the microemulsion which coexists at high temperatures with an excess water phase is a water-in-oil-droplet microemulsion while at low temperatures it is an oil-in-water-droplet microemulsion that coexists with the oil excess phase. Furthermore, it is self-evident that the microemulsion's microstructure does not change all of a sudden but continuously with the temperature. When the temperature increases the mean curvature $H$ changes from positive to negative values and runs through zero, notably, just at the temperature $\widetilde{T}$. Consequently, microemulsions are bicontinuous at (and, a little less ideally, also around) their $\widetilde{T}$ temperature. This fact was made use of throughout this work. To investigate the microemulsions in the bicontinuous state and in the absence of excess phases samples were prepared with a surfactant mass fraction $\gamma$ slightly above $\widetilde{\gamma}$, then they were studied at or close to $\widetilde{T}$. To facilitate the measurements, i.e. to avoid phase separation upon small temperature fluctuations during the sample handling, the surfactant mass fraction was usually chosen about 2–5 wt% above $\widetilde{\gamma}$. There the one-phase temperature region between $T_{\underline{2}-1}$ and $T_{1-\underline{2}}$ is wider than close to the $\widetilde{X}$ point. However, one must be aware that the bicontinuous microstructure which is ideal at $\widetilde{\gamma}$ is altered the stronger the more the surfactant mass fraction is increased above $\widetilde{\gamma}$. The additional surfactant leads to a stiffening of the surfactant film which is thus less curved such that the water and oil domains are enlarged. Eventually the surfactant film is so rigid that a lamellar liquid crystalline structure is formed. Such high surfactant mass fractions, however, were obviated for the measurements in this thesis.

## 2.2  Base System 2: Binary Gel

The second base system of the gelled bicontinuous microemulsion $H_2O$–$n$-decane/12-HOA–$C_{10}E_4$, which is studied in this thesis, is a "simple" gel of the gelator 12-HOA in which the solvent is not a complex fluid like the bicontinuous microemulsion but an ordinary liquid. Which type of liquid is suitable follows from the chemical structure of 12-HOA (see Fig. 2.6). The latter is a hydroxylated fatty acid, also called 12-hydroxystearic acid, which is a hydrogenation derivative of castor oil and industrially used, e.g., as thickener in lubrication greases [26, 27]. Its "thickening effect" is based on a spontaneous aggregation (self-assembly) of the 12-HOA molecules in solution which can be seen as micro-phase separation of the gelator from the solvent [28]. This micro-phase separation competes with the gelator's solubility in the liquid. Given that both effects are balanced a gel is formed [29, 30]. In the case of 12-HOA this is normally found when the solvent is a non-polar "oil" like, e.g., an $n$-alkane, cyclohexane or benzene. Therefore one classifies 12-HOA as 'organogelator', as opposed to 'hydrogelators' which gel aqueous solutions [31].

**Fig. 2.6** Molecular structure
of 12-hydroxyoctadecanoic
acid (12-HOA)
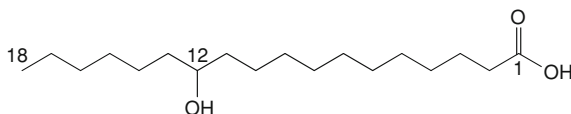


For the thesis at hand it was reasonable to work with *n*-decane as solvent in the 12-
HOA gel since this substance was also contained in the investigated microemulsion.
Further components were not needed for gel formation, hence the system *n*-decane/
12-HOA is often referred to as the "binary gel" in this work. Since the major
constituent of a gel is always the solvent [32] the gelator concentration in the studied
gels was 1.5, 2.5 wt% and at the most 5.0 wt%. Note that 12-HOA is a chiral
molecule due to the hydroxy group at C-atom 12 (see Fig. 2.6).

### 2.2.1 12-HOA as Low Molecular Weight Organic Gelator Building Physical Gels

As a carbon compound with a molecular weight of 330.48 g mol$^{-1}$ 12-HOA is
reckoned among the so-called 'low molecular weight organic gelators' (LMOGs)
which make up 'molecular gels' [31]. LMOGs are "gelators that are primarily
organic in composition and whose molecular mass is usually less than 2,000 Da"
[29]. They can be distinguished from polymeric gelators, like gelatin or poly-
acrylamide, which are much bigger building blocks for the formation of the three-
dimensional gelator network that is found in every gelled system. Thus, another
classification for gels is based on the nature of the bonds between the building
blocks and in the junctions of the gelator network. When these bonds are covalent
one speaks of 'chemical gels' [32]. In 'physical gels', by contrast, those bonds are
non-covalent, like, e.g., van-der-Waals interactions, hydrogen or ionic bonds. As a
consequence physical gels show a thermoreversible phase-behaviour [28, 29,
32–34]. When they are heated up above a certain temperature they 'melt' and a
low-viscous 'sol', i.e. an isotropic solution of freely diffusing gelator molecules, is
formed. Cooled down below the 'sol-gel transition temperature' $T_{\text{sol-gel}}$, the gelator
molecules self-assemble (again) and the mixture (re-)gels. The temperature of the
'sol-gel boundary' is the higher the higher the gelator concentration, however, it
levels off at some point [29] as can be seen in the schematic temperature-com-
position phase diagram shown in Fig. 2.7. Note that due to the different interac-
tions which stabilize the gelator network in a physical gel the sol-gel transition
happens not at a certain point but within a certain temperature range, thus one also
speaks of a sol-gel "transition zone".

   In chemical gels the situation is different. Their strong covalent bonds do not
loosen at elevated temperatures like the non-covalent bonds in physical gels.
Hence chemical gels undergo irreversible degradation when they are overheated.
Moreover, chemical gels possess a special swelling behaviour due to their

**Fig. 2.7** Schematic representation of a temperature versus gelator concentration phase diagram of a physical gel. The test tubes above and below the sol-gel boundary illustrate the respective states of the solvent/gelator mixture
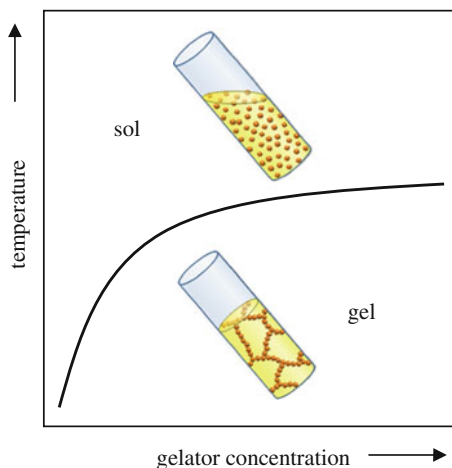


permanent bonds which is even used for a gel definition in the Dictionary of Polymers [35]. There it is stated that a covalently linked polymer gel "swells in a solvent to a certain finite extend, but does not dissolve even in a good solvent". Physical gels, in contrast, can dissolve or rather do not form if the solvent concentration is too high or the gelator concentration too low, respectively [32].

### 2.2.2  Structure of 12-HOA Gels

From a topological point of view gels consist of a three-dimensional network which is infinitely extended throughout the whole system and swollen by an embodied solvent [36]. While chemical gels possess discrete connection points in the gelator network one finds in physical gels rather extended 'junction zones' of the gelator strands [37]. In molecular gels the latter are the primary structures formed when the low molecular weight gelator (LMG) molecules self-assemble [31]. This happens upon cooling of the sol which yields a supersaturated mixture wherein a nucleation process initiates. The formed microcrystallites grow preferentially in one dimension such that elongated structures like, e.g., rods or tubes develop [31]. These eventually branch and/or associate building the secondary three-dimensional so-called 'self-assembled fibrillar network' (SAFIN). In the case of 12-HOA one finds dimers of the gelator molecules (pairing their carboxylic acid groups) across the fiber section while hydrogen bonds between the hydroxy groups are the dominating interactions in the direction of the fiber axis [34, 38] (see Fig. 2.8). Moreover, hydrogen bonds can be formed between two neighbouring gelator fibers which expose their hydroxy groups to the fiber surface [39]. This happens in the so-called 'non-permanent' or 'transient junction zones' of 12-HOA networks while the 'permanent junction zones' are branch points of the fibers which arise because of crystallographic mismatches during fiber growth [40].
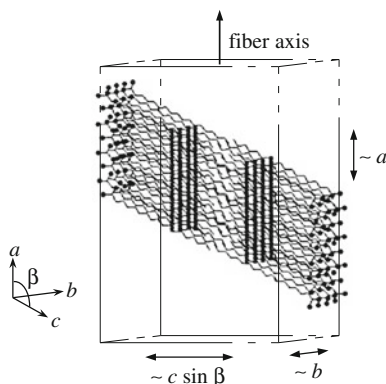
Notably the shape and size of the gelator fibers and junction zones is very much
dependent on the molecular structure of the gelator [29, 41], on the type of the
solvent in the gel [29, 30, 38, 42], on the presence of additives [43] and on the
cooling rate upon gel formation [42, 44, 45]. In 12-HOA gels one finds gelator
fibers whose cross-section is, e.g., square when the solvent is benzene and rect-
angular in nitrobenzene where the 12-HOA strands are ribbon-shaped [38]. As
regards dimensions, the thickness of gelator fibers is usually in the nanometer
range while their length can be of several micrometers. Note that the crystalline
packing of the gelator molecules within the gelator fibers differs from the packing
in a neat gelator crystal [37, 46]. Another difference between neat gelator crystals
and gels is that the former are thermodynamically stable systems while the latter
are, though they are long-lived, not in an equilibrium state [47].

## 2.2.3 Mechanical Properties of Gels

When it comes to properties, it is remarkable that though consisting predominantly
of a liquid a gel shows a solid-like behaviour [32]. This can be ascribed to the
rather rigid (in SAFINs crystalline) gelator fibers and their cross-linking, espe-
cially in the permanent junction zones or connection points. The gelator network
thus "arrests" the solvent molecules and gives rise to the gel's mechanical sta-
bility. The latter is the basis for phenomenological gel definitions like the claimed
"self-supporting ability" of gels and the statement that "a gel does not flow" [32].
However, attempting to experimentally test this for a system under investigation
one directly faces the questions which environmental conditions to use and how
long to wait for a flow of the potential gel. Unfortunately there are no definite
answers to these questions—in principle one should observe the sample forever.
Yet in practice there is of course always a limit for the timescale of observation.
Thus it becomes evident that a gel is "easier to recognize than to define" as
Dr. Dorothy Jordan Lloyd already realized in 1926 [48]. An approach to quantify

the solid-like behaviour of gels is to study their rheological properties. Gelled systems are viscoelastic, i.e. they show both characteristics of Hookean solids (elasticity) and of Newtonian liquids (viscosity) [32]. Therefore gels are in an intermediate state in between a solid and a liquid. The rheological parameters representing elasticity and viscosity are the storage modulus $G'(\omega)$ and the loss modulus $G''(\omega)$, respectively, as will be explained in detail in the following Sect. 2.3. These parameters are measureable, however, there is again a limit of observation which is in this case the lowest (angular) frequencies $\omega$ that are accessible by a state-of-the-art rheometer. With the aim to give another, applicable gel definition Almdal et al. specified that "solid-like gels are characterized by the absence of an equilibrium modulus, by a storage modulus, $G'(\omega)$, which exhibits a pronounced plateau extending to times at least of the order of seconds, and by a loss modulus, $G''(\omega)$, which is considerably smaller than the storage modulus in the plateau region" [49].

## 2.3 Rheology

Rheology comes from the Greek word 'rheos' which means 'flow'. Flow, which is nothing but the continuous deformation of a material, occurs as a reaction to experienced stress. Thus, rheology deals with the deformation behaviour of materials which reveals characteristic properties of the latter. For example, squeezing a rubber ball and a piece of dough causes completely different 'responses' from the probed materials and it is indeed these responses that are described, measured and interpreted in rheometrical studies. The basics of rheology have been described in numerous textbooks, like Refs. [50–55], of which the theory relevant for the thesis at hand is explained in this chapter.

### 2.3.1 Basic Definitions

All rheometry experiments carried out for this work were oscillating shear rheometry measurements. **Shear** deformation of an object is associated to a **shear stress** $\tau$ which results from a force $\boldsymbol{F}$ (of magnitude $F$) directed parallel to one of the object's surfaces $A$

$$\tau = \frac{F}{A}.\tag{2.7}$$

   This is illustrated in Fig. 2.9 where a sample is sheared between two plates of distance $z$ the lower of which remains stationary while the upper plate is moved by a distance $x$.

**Fig. 2.9** Shearing a sample
between two plates of
distance $z$ by moving the
upper plate of area $A$ with a
force $\boldsymbol{F}$ by the distance $x$
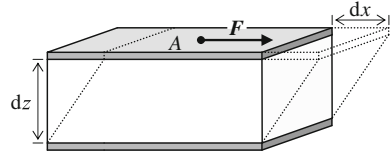


The **shear strain** experienced by the sample is defined as

$$\gamma = \frac{\mathrm{d}x}{\mathrm{d}z}. \tag{2.8}$$

Also important is the **shear rate**, i.e. the shear strain per time unit $\mathrm{d}t$, which is
equivalent to the shear velocity $v$ (i.e. the shear displacement $\mathrm{d}x$ per time unit) at
gap width $\mathrm{d}z$

$$\dot{\gamma} = \frac{\gamma}{\mathrm{d}t} = \frac{\mathrm{d}x/\mathrm{d}z}{\mathrm{d}t} = \frac{\mathrm{d}x/\mathrm{d}t}{\mathrm{d}z} = \frac{v}{\mathrm{d}z}. \tag{2.9}$$

## 2.3.2 Elastic, Viscous and Viscoelastic Materials and Their Rheologic Behaviour

Different materials react differently when exposed to a (shear) stress. In general,
one distinguishes between **elastic** solids and **viscous** liquids. If an elastic solid is
deformed an internal restoring force arises which brings the material back to its
initial shape once the external force is released. Thus the deformation is reversible
like, e.g., in a spring. According to Hooke, there is a linear proportion between the
deformation of the object and the magnitude of the force. Applying this to shear
deformations one introduces the shear modulus

$$G = \frac{\mathrm{d}\tau}{\mathrm{d}\gamma} \tag{2.10}$$

as proportionality constant between the shear stress $\tau$ and the shear strain $\gamma$.

If one, by contrast, deforms a viscous liquid the deformation is irreversible
since the counterforce to the external force is not a restoring but a frictional force
between the particles in the fluid. This is the case, e.g., in a dashpot. The friction is
the greater the faster the fluid is deformed. Thus, according to Newton, the shear
stress $\tau$ in a shear deformation is linearly proportional to the shear rate $\dot{\gamma}$. The
proportionality constant

$$\eta = \frac{d\tau}{d\dot{\gamma}} \tag{2.11}$$

is called the dynamic viscosity of the fluid. This characteristic property can be measured in **stationary**, i.e. **time-independent**, **rheometry** experiments like rotational measurements. One shears the sample with a certain shear rate and determines the respective shear stress. For an ideal Newtonian liquid one single measurement would be enough since its $\tau - \dot{\gamma}$ curve is linear. However, for real liquids Newtonian behaviour is usually found for small shear rates only, i.e. for slow shearing or thick sample layers. At higher shear rates one often observes shear-thinning or shear-thickening behaviour like, e.g., in 'solid paint' and starch suspensions, respectively. Accordingly, one measures non-linear flow curves for such "non-Newtonian" liquids which are described by different more complex models as Newton's simple model is not valid any more. Also temperature has an effect on the dynamic viscosity of a fluid. One finds that $\eta$ decreases for liquid samples with increasing temperature while it increases for gases.

Some, so-called 'plastic' materials appear as solids below a certain yield stress $\tau_B$ while above they are liquid-like and flow. This is described by the Bingham model

$$\tau = \eta_B \, \dot{\gamma} + \tau_B \tag{2.12}$$

in which $\eta_B$ is the plastic viscosity.

Note that a material in a stationary rheometry experiment behaves either as an elastic solid, which reversibly deforms up to a certain point under the experienced stress, or as a viscous fluid, which continuously flows and thus deforms irreversibly under the stress. Many materials, however, do possess both elastic and viscous properties. They are called **viscoelastic** and can be represented by a connection of a spring and a dashpot as, e.g., in the **Kelvin-Voigt model** (connection in parallel; Fig. 2.10, left top) or in the **Maxwell model** (connection in series; Fig. 2.10, left bottom). When a continuous stress is applied these models exhibit solid-like (Kelvin-Voigt model) or liquid-like (Maxwell model) behaviour. However, if stress is applied only temporarily the models' behaviour is more complex. For example, when stress is applied on the Maxwell model between a time $t_0$ and a time $t_1$ (Fig. 2.10, right top) this leads initially to a deformation $\Delta\gamma$ of the spring and between $t_0$ and $t_1$ to a continuous deformation of the dashpot with a rate $\dot{\gamma}$ (Fig. 2.10, right bottom). The dashpot deformation immediately stops once the stress is released at $t_1$ where furthermore the spring resets by $-\Delta\gamma$ to its undeformed state. This leaves the system with a total deformation of $\gamma_1 = \dot{\gamma}(t_1 - t_0)$. Note that it is possible to deduce both the spring constant (from $\Delta\gamma$) and the viscosity of the dashpot fluid (from $\dot{\gamma}$) from the obtained $\gamma$–$t$ curve. Thus, this example demonstrates that when the applied stress in a rheometry experiment is varied as a function of time it is possible to simultaneously yield information on the solid-like and the liquid-like properties of the probed material. Therefore, **non-stationary**, i.e. **time-dependent**, **rheometry** experiments are normally used to study viscoelastic samples like the gelled microemulsions in this thesis.
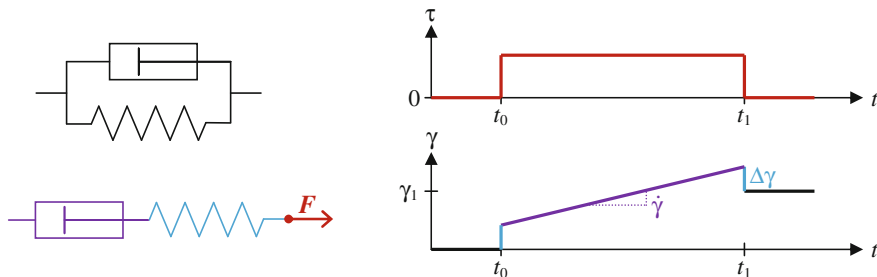
**Fig. 2.10** Kelvin-Voigt model (*left top*) and Maxwell model (*left bottom*) for viscoelastic materials. (*Right*) Stress $\tau$ and strain $\gamma$ versus time $t$ curves for the described experiment with the Maxwell model

## 2.3.3 Studying Viscoelastic Materials with Non-Stationary Rheometry

If one investigates a viscoelastic material with time-dependent rheometry it is important to be aware of the great impact of (a) the applied stresses and (b) the timescale of observation. This shall be illustrated on the basis of the experiment with the Maxwell model described above (see Fig. 2.11, cp. Fig. 2.10, bottom right).

As it is shown in Fig. 2.11 (left) an increase of the stress $\tau$, which is applied at $t_0$ and released at $t_1$, linearly increases the spring deformation $\Delta\gamma$. Since the spring deformation allows characterizing the solid-like properties of the studied material a sufficiently high stress should be chosen to yield a significant $\Delta\gamma$ value. However, if the applied stress is too high the spring is damaged and loses its linear Hookean elasticity which precludes obtaining reasonable results. In a complex fluid this corresponds to an alteration of the system's microstructure by the high stresses which, aiming to probe the original system, one normally seeks to avoid. Therefore, the so-called "**linear viscoelastic (LVE) range**" is usually determined within the first experiments.

To be able to characterize the liquid-like properties of a material, which in the described experiment requires the reliable determination of the slope $\dot\gamma = \Delta_{\text{flow}}\gamma/\Delta t = \gamma_1/\Delta t$, it is important to observe the sample deformation over a sufficiently long time span $\Delta t = t_1 - t_0$ (cp. Fig. 2.11, right). Especially when the slope is very small, i.e. when the viscosity of the dashpot fluid is high and it takes a long time for the dashpot to deform, it is the more difficult to notice that $\gamma_1$ differs from zero the shorter the observation time $\Delta t$. However, if no slope and, respectively, no flow are observed this misleadingly implies that the probed model does not consist of a spring and a dashpot but of a spring only. In other words, recognizing the liquid-like properties of a viscoelastic material and thus distinguishing it from a solid material can take a very long time. At this point rheology can even become philosophic. The saying "panta rhei" (Greek) which is ascribed to Heraclitus who
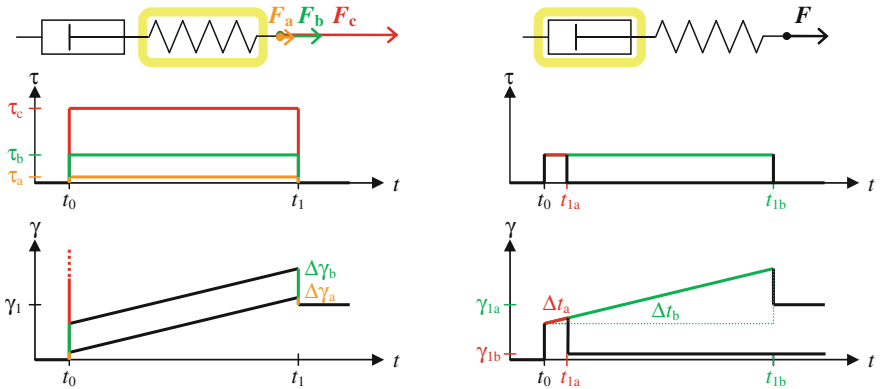
**Fig. 2.11** Impact of the applied stress (*left*) and the timescale of observation (*right*) on the described non-stationary rheometry experiment with the Maxwell model

lived around 500 BC means "**everything flows**"; from a rheological point of view one might complement: it is just a matter of time [51]. An example of a very slowly flowing material which appears solid when observed at room temperature for just a minute, an hour or even a day is the resin pitch. However, the famous pitch drop experiment demonstrates that pitch does possess liquid-like properties: it drops out of a funnel, but only once every 7–12 years (observation period: 1930–2013) [56–58]. In short, while fast (instantaneous) stress variations expose the elastic properties of viscoelastic materials long observation times are preferable to reveal the viscous behaviour. Accordingly, it is beneficial to study a sample on both short and long timescales in a rheometry experiment, being aware that there is always a practical limit of observation as regards the long timescales.

### 2.3.4  Oscillating Shear Rheometry

A non-stationary method with which one can probe a sample on different time-scales is oscillating shear rheometry. In such experiments one applies an alternating shear stress the maximum amplitude of which is within the LVE region. The frequency of the stress variation and thus of the shear deformation corresponds to the inverse timescale of observation. At low frequencies where the sample is sheared slowly the viscoelastic material has enough time to flow while it behaves predominantly elastic when sheared fast at high frequencies. If the shear strain $\gamma$ is sinusoidal and oscillates as a function of time $t$ with the frequency $f$—or, respectively, with the angular frequency $\omega = 2\pi f$—and the maximum amplitude $\gamma_{max}$
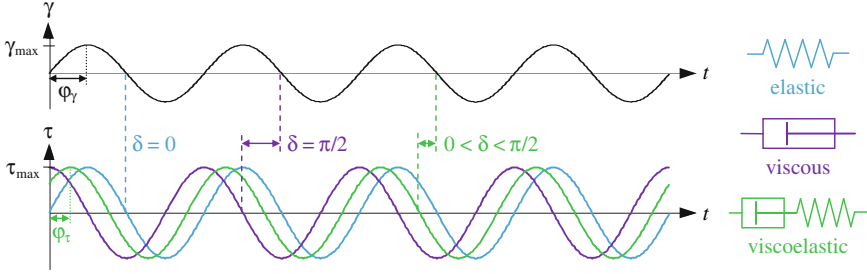
**Fig. 2.12** Sinusoidal shear strain (*top*) and stress responses of different materials (*bottom*)

$$\gamma(t) = \gamma_{\max} \sin(\omega t) \qquad (2.13)$$

the shear stress $\tau_{\text{elastic}}$ in an ideal elastic solid is, according to Hooke, completely in phase with this deformation (phase shift $\delta = 0$) and thus

$$\tau_{\text{elastic}}(t) = \tau_{\max} \, \gamma(t) = \tau_{\max} \, \sin(\omega t) \qquad (2.14)$$

with the maximum amplitude $\tau_{\max}$ (cp. Fig. 2.12, blue). In an ideal viscous fluid, by contrast, the shear stress $\tau_{\text{viscous}}$ is, according to Newton, proportional to the shear rate, i.e. to the shear strain differentiated with respect to the time. Thus it is not in phase with $\gamma(t)$ but cosinusoidal

$$\tau_{\text{viscous}}(t) = \tau'_{\max} \, \dot{\gamma}(t) = \tau'_{\max} \frac{d(\gamma_{\max} \sin(\omega t))}{dt} = \tau'_{\max} \, \omega \, \cos(\omega t) = \tau_{\max} \, \cos(\omega t)$$
$$(2.15)$$

which means phase shifted by $\delta = \pi/2$ (cp. Figure 2.12, purple). When a material is viscoelastic the combination of the elastic and the viscous contributions leads to a phase shift between $\gamma(t)$ and $\tau(t)$ of $0 \leq \delta \leq \pi/2$ (cp. Fig. 2.12, green). This phase shift can be measured and is characteristic for the studied material. The second parameter which is needed to fully characterize the relationship between the shear stress and the strain response of a sample is the ratio between the amplitudes $\tau_{\max}$ and $\gamma_{\max}$. This ratio is called the **complex modulus**

$$|G^*| = \frac{\tau_{\max}}{\gamma_{\max}} \qquad (2.16)$$

and interpreted as the absolute value of a complex number $G^*$ which is by definition [50]

$$G^*(\omega) \equiv \frac{\tau^*(\omega)}{\gamma^*(\omega)}. \qquad (2.17)$$

Thus, $G^*$ can be seen as proportionality constant between $\tau^*$ and $\gamma^*$ at the angular frequency $\omega$, in analogy to the shear modulus definition in Eq. (2.10). The introduction of complex numbers for the description of shear oscillations is simply for reasons of mathematical handiness. The complex numbers allow, e.g., the separation of $G^*$ in a real and an imaginary component called the **storage modulus $G'$** and the **loss modulus $G''$**

$$G^*(\omega) = G'(\omega) + i\, G''(\omega). \tag{2.17a}$$

As will shortly be evidenced these moduli represent the elastic and the viscous contribution to a viscoelastic material's behaviour (elastic solids *store* applied energy through restoring forces while the energy is *lost* in viscous fluids due to friction). To understand how $G'$ and $G''$ can be determined it is convenient to express the complex number $G^*$ in Euler's notation for which also the shear stress and the shear strain must be expressed as complex functions according to Euler. Thus instead of using sinus or cosine one writes for the oscillating shear stress

$$\tau^*(\omega) = \tau_{max}(\cos(\omega t + \varphi_\tau) + i\, \sin(\omega t + \varphi_\tau)) = \tau_{max}\, e^{i(\omega t + \varphi_\tau)} = \tau_{max}\, e^{i\omega t}\, e^{i\varphi_\tau} \tag{2.18}$$

and for the oscillating shear strain

$$\gamma^*(\omega) = \gamma_{max}\big(\cos(\omega t + \varphi_\gamma) + i\, \sin(\omega t + \varphi_\gamma)\big) = \gamma_{max}\, e^{i(\omega t + \varphi_\gamma)} = \gamma_{max}\, e^{i\omega t}\, e^{i\varphi_\gamma} \tag{2.19}$$

in which $\omega$ is the angular frequency and $\varphi_\tau$ and $\varphi_\gamma$ are the initial phase angles the difference of which yields the phase shift

$$\delta = \big|\varphi_\tau - \varphi_\gamma\big|. \tag{2.20}$$

Note that the imaginary parts of $\tau^*(\omega)$ and $\gamma^*(\omega)$ are irrelevant in practice while the real parts correspond to the time-dependent equations specified above, e.g. Eq. (2.13) which is yielded as real part of Eq. (2.19) if $\varphi_\gamma = -\pi/2$

$$\mathrm{Re}(\gamma^*(\omega)) = \gamma_{max}\, \cos(\omega t + \varphi_\gamma) = \gamma_{max}\, \cos(\omega t - \pi/2) = \gamma_{max}\, \sin(\omega t) = \gamma(t). \tag{2.13a}$$

If one now puts the expressions (2.18) and (2.19) in Eq. (2.17) one can calculate $G^*$ as

$$G^*(\omega) = \frac{\tau_{max}\, e^{i\omega}\, e^{i\varphi_\tau}}{\gamma_{max}\, e^{i\omega}\, e^{i\varphi_\gamma}} = \frac{\tau_{max}}{\gamma_{max}}\, \frac{e^{i\varphi_\tau}}{e^{i\varphi_\gamma}} = |G^*|\, e^{i\delta}. \tag{2.17b}$$

**Fig. 2.13** Visualization of
$G^*$ in the complex plane
where Im is imaginary and Re
the real axis
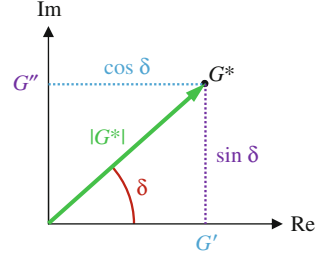


To eventually clarify the relationship between the complex modulus $|G^*|$, the
phase shift $\delta$, which is determined in the measurement, and the storage and loss
moduli $G'$ and $G''$, which represent a viscoelastic material's solid-like and liquid-
like properties, respectively, one can visualize $G^*$ in the complex plane (Fig. 2.13)
[51, 54].

Trigonometrical laws now directly reveal the equations

$$G'(\omega) = |G^*| \, \cos \delta \tag{2.21}$$

and

$$G''(\omega) = |G^*| \, \sin \delta \tag{2.22}$$

according to which the storage modulus $G'$ and the loss modulus $G''$ are calculated
in a rheometry experiment. Note that $G'$ and $G''$ have the same unit as the complex
modulus $|G^*|$ which originates from $\tau_{max}$ as one can see in Eq. (2.16) and is thus
pascals. The assignment of these two moduli to elastic and viscous behaviour,
respectively, becomes obvious when one puts into the Eqs. (2.21) and (2.22) the
two possible boundary values for the phase shift between the stress and the strain
oscillation, i.e. $\delta = 0$ and $\delta = \pi/2$. As explained above, stress and strain are in
phase for an elastic solid. Thus with $\delta = 0$ one obtains $[G'(\omega)]_{\text{elastic},\delta=0} = |G^*|$ and
$[G''(\omega)]_{\text{elastic},\delta=0} = 0$ which shows that the loss modulus vanishes for perfect
elasticity. The opposite is true for perfectly viscous fluids in which stress and strain
are out of phase by $\delta = \pi/2$. Here one obtains $[G'(\omega)]_{\text{viscous},\delta=\pi/2} = 0$ and
$[G''(\omega)]_{\text{viscous},\delta=\pi/2} = |G^*|$, respectively. In general, it holds for viscoelastic
materials that they behave the more solid-like the bigger the storage modulus in
comparison to the loss modulus, i.e. the smaller the 'loss factor'

$$\frac{G''}{G'} = \tan \delta. \tag{2.23}$$

Note that for defined models such as the Maxwell or the Kelvin-Voigt model
one can form constitutive equations which unequivocally relate stress and strain.
Based on such an equation it is possible to find explicit expressions for $G'(\omega)$ and

$G''(\omega)$ which depend on characteristic parameters of the sample like the shear modulus and the dynamic viscosity. Thus, data measured in a rheometry experiment can be fitted to these expressions in order to yield the characteristic quantities as fit parameters. Moreover, the quality of the fit indicates whether the applied model is appropriate for the studied sample. Many viscoelastic materials, however, possess an intricate rheological behaviour and cannot be described by simple models. Thus complex models have been developed which are, e.g., based on different interconnections of numerous Hookean springs and Newtonian dashpots.

### 2.3.5 Stress-Controlled Shear Rheometer

In non-stationary rheometry experiments one usually determines the storage modulus $G'$ and the loss modulus $G''$ as a function of the frequency. For the thesis at hand this was accomplished through oscillation measurements on a stress-controlled shear rheometer with a plate–plate geometry. In such a rheometer the sample is placed between two circular plates of distance $z$ the lower of which is stationary while the upper plate, which has a radius $R$, is moved via an electric motor (Fig. 2.14). The generated movement is rotative around the plate's center axis, in contrast to the linear displacement assumed above where the basic parameters of shear deformation were introduced. Therefore, shear stress and shear strain must be translated to parameters which are used for describing circular motion.

Shear stress, according to Eq. (2.7), is the force $F$ applied on an area $A$. In circular motion a force of magnitude $F$ which takes effect at a distance $r$ from the axis gives rise to a momentum of force (torque) $\boldsymbol{M}$ of magnitude

$$M = F\,r. \tag{2.24}$$

On the moving plate of the rheometer force affects each area element $\mathrm{d}A$, which, through differentiation of a circular area of radius $r$, can be expressed as

$$\mathrm{d}A = 2\pi\,r\,\mathrm{d}r. \tag{2.25}$$

Thus, if one applies the torque $M$ on a circular rheometer plate of radius $R$ the sample experiences the shear stress

$$\tau = \frac{F}{\mathrm{d}A} = \frac{M}{2\pi\,r^2\,\mathrm{d}r} = \frac{M}{2\pi\,\int_0^R r^2\,\mathrm{d}r} = \frac{3\,M}{2\pi\,R^3}. \tag{2.7a}$$

Inversely, a converted form of Eq. (2.7a) can be use to determine the torque $M(\omega, t)$ that an electromotor must produce in order to exert a specified oscillating shear stress $\tau(\omega, t)$ of angular frequency $\omega$ on a sample between the rheometer plates.
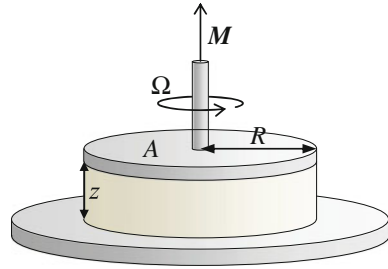
The measured quantity in a stress-controlled rheometer is the shear strain which
is the ratio of the shear deformation to the gap width (cp. Eq. 2.8). The shear
deformation is specified as the circular arc, which is of course different for dif-
ferent radii; however, it is the convention to quote the arc for the plate radius $R$. To
calculate the arc one needs the angle of rotation $\alpha$ which is measured by a dis-
placement sensor. Thus one yields the shear strain as

$$\gamma = \frac{dx}{dz} = \frac{R\,\alpha}{z}. \tag{2.8a}$$

Note that besides stress-controlled there are also strain-controlled shear rhe-
ometers which work according to the inverse concept: a certain shear strain $\gamma(\omega, t)$
is applied and the resulting shear stress $\tau(\omega, t)$ is measured. As regards the mea-
surement geometry apart from plate–plate assemblies one also uses cone–plate
systems in which the moving element is not an even plate but a shallow cone
(angle $\leq 4°$). The advantage of using a cone is that the shear rate at an angular
velocity $\Omega$ is uniform across the gap while in a plate–plate system $\dot{\gamma}$ depends also
on the radius $r$

$$\dot{\gamma} = \frac{\gamma}{dt} = \frac{r\,d\alpha/dt}{dz} = \frac{r\,\Omega}{dz}. \tag{2.9a}$$

An even shear velocity distribution is desirable particularly in stationary rota-
tional shear rheometry experiments. However, for the present study with non-
stationary oscillating shear rheometry experiments the plate–plate assembly was
preferable since it allows adjusting the gap width to the needs of the sample which
is not possible in a cone–plate system.

## 2.4 Fourier Transform Pulsed-Gradient Spin-Echo NMR Spectroscopy

Fourier transform pulsed-gradient spin-echo (FT-PGSE) nuclear magnetic reso-
nance spectroscopy, also known as pulsed field gradient NMR or PFG-NMR, is a
sophisticated technique for studying translational diffusion processes. The basic

principle is to measure the attenuation of the spin-echo signal in an NMR spin-echo experiment, during which pulses of a defined magnetic field gradient are applied. As the echo attenuation is induced by the displacement of the spin in the direction of the gradient the self-diffusion coefficient of the corresponding molecule can be computed. A great benefit of the Fourier transform variant of the PGSE NMR method is that it allows determining simultaneously self-diffusion coefficients of different components in one sample. This is possible since Fourier transforming the generated echo signal yields multiple signals in the frequency domain which can be assigned to the different species in the sample according to their chemical shifts. Consequently, one can follow the attenuation of each signal separately and obtains the individual self-diffusion coefficients $D$, e.g. of water and oil in a microemulsion. Another advantage of the FT-PGSE NMR technique is that it is non-invasive and non-destructive, i.e. neither the sample composition needs to be changed (e.g. by adding tracer molecules) nor is the sample destroyed by the measurement [59].

## 2.4.1 Fundamentals of Self-Diffusion and NMR Spectroscopy

Self-diffusion is the most fundamental transport mechanism of molecules and particles in fluid systems [60]. It results from random-walk processes due to thermal motion and leads to a radial Gaussian distribution of particles which all started at time $t = 0$ in the position $\boldsymbol{r_0}$ of an infinitely large, isotropic, homogeneous system. The probability to find one of the particles at time $t$ in the position $\boldsymbol{r}$ is thus [61]

$$P(\mathbf{r_0}, \mathbf{r}, t) = (4\pi Dt)^{-3/2} \, e^{-\frac{(\mathbf{r}-\mathbf{r_0})^2}{4Dt}}. \tag{2.26}$$

This equation reveals that the self-diffusion process is fully described by the parameter $D$, i.e. the self-diffusion coefficient which is measured in the PGSE NMR experiment. The average displacement of particles via self-diffusion is zero. However, for the mean square displacement it holds

$$\left\langle |\boldsymbol{r} - \boldsymbol{r_0}|^2 \right\rangle = \left\langle r^2 \right\rangle = nDt \tag{2.27}$$

and the root mean square displacement is

$$\sqrt{\langle r^2 \rangle} = \sqrt{nDt} \tag{2.28}$$

in which $n = 2$, 4 or 6 for one-, two- or three-dimensional displacement, respectively. Equation (2.27) states that the mean square displacement of a self-diffusing molecule scales linearly with time which is what one finds in samples of

neat substances. The self-diffusion coefficient measured in the case of free self-diffusion is denoted $D_0$ and for low viscous solvents (e.g. water, alkanes) it lies in the order of $10^{-9}$ m$^2$ s$^{-1}$. However, when the self-diffusing molecules encounter obstruction within the observation time the situation is different. If, for example, an additional compound is present which forms aggregates or encloses itself in a solvation shell this can slow down the effective motion of the investigated molecules. Consequently, a reduced self-diffusion coefficient $D$ is measured which therefore contains structural information about the sample. Note that studying the microstructure of microemulsions via FT-PGSE NMR spectroscopy is possible particularly for this reason as will later be explained in detail.

If a sample is placed in a static and homogeneous magnetic field $\boldsymbol{B}$, as it is the case in an NMR spectrometer, the magnetic moments $\boldsymbol{\mu}$ associated to nuclear spins $\boldsymbol{I} \neq 0$ account for a net magnetisation $\boldsymbol{M}$ which is aligned parallel to the field. This happens due to the quantization of spin states which allows for a spin only $2I + 1$ orientations (specified as $m_I = -I, -I + 1, \ldots, I$) with respect to an arbitrary axis, i.e. the direction of the magnetic field, usually referred to as the $z$-direction. The magnetic field causes energy level splitting for the different spin orientations which in case of protons ($I_{\text{proton}} = \frac{1}{2}$) results in slightly more low-energy 'α-spins' ($m_I = \frac{1}{2}$) than high-energy 'β-spins' ($m_I = -\frac{1}{2}$). According to Boltzmann the ratio of the populations of the different energy levels in thermodynamical equilibrium is given by

$$\frac{N_\beta}{N_\alpha} = e^{-\frac{\Delta E}{k_B T}} \tag{2.29}$$

where $N_\alpha$ and $N_\beta$ are the numbers of α-spins and β-spins, respectively, $k_B$ is the Boltzmann constant, $T$ the absolute temperature and $\Delta E$ the energy difference between the two spin states. The latter is directly proportional to the strength of the magnetic field $B$ and can be overcome, i.e. spin reorientation can be induced, by irradiation of the resonance frequency $\nu_L$, the so-called Larmor frequency. It holds

$$\Delta E = \hbar\, \gamma_g\, B = h\, \nu_L \tag{2.30}$$

where $h$ is the Planck constant ($h = 2\pi\hbar$) and the coefficient $\gamma_g$ is the gyromagnetic ratio which is characteristic for the respective nucleus (e.g. proton: $\gamma_{g,\text{pr.}} = 2.675 \times 10^8$ s$^{-1}$ T$^{-1}$ [62]). For example, in a magnetic field of 9.4 Tesla the Larmor frequency of protons is 400.2 MHz (hence, an NMR instrument with such a magnetic field is called a '400 MHz spectrometer'). To picture the energy difference between the spin states the spins are usually described as precessing with their Larmor frequency around the direction of the magnetic field. Therefore, the $x$- and $y$-components $\mu_x$ and $\mu_y$ of all magnetic moments in the sample cancel out while the $z$-components $\mu_z$ sum up to the net magnetisation $\boldsymbol{M}$ in the direction of the magnetic field $\boldsymbol{B}$. By irradiating radio frequency pulses the sample can be excited which generates oscillating $x$- and $y$-components of the magnetisation $M_x(t)$ and $M_y(t)$. These magnetisation components, in turn, induce the measured

signal in the detector coil which is located in the $xy$-plane. As the spins relax to thermodynamic equilibrium the detected signal decays exponentially for which it is referred to as 'free induction decay' or 'FID signal'. In general, two relaxation processes are distinguished. Firstly, the spins flip their orientations and re-establish the equilibrium populations of the $\alpha$- and $\beta$-energy levels (see Eq. 2.29) with a time constant $T_1$ which is called the longitudinal or spin–lattice relaxation. Secondly, the spins lose their phase coherence with a time constant $T_2$ due to different precession velocities induced by fluctuating fields which is referred to as transversal or spin–spin relaxation.

### 2.4.2 Principle of the PGSE NMR Experiment

In general, PGSE NMR experiments are based on radio frequency pulse sequences which induce a so-called 'spin-echo' signal. The easiest example is the $[\pi_x/2 - \tau - \pi_x - \tau]$ sequence, commonly referred to as 'Hahn echo' [63], which is depicted in Fig. 2.15.

The first $\pi_x/2$-pulse in the Hahn spin-echo experiment rotates the magnetisation in the $xy$-plane after which an FID signal is observed as the spins dephase because they possess different Larmor frequencies. This is predominantly due to inhomogeneities of the magnetic field $\boldsymbol{B}$ of the spectrometer. In order to eliminate this experimental effect and to follow the pure spin–spin relaxation process, a second radio frequency pulse ($\pi_x$-pulse) is irradiated after a time period $\tau$. This pulse is twice as long as the first one and inverts the spin positions. Now the ongoing precession of the spins refocuses them which leads to an echo signal of the FID at time $2\tau$. Comparing the intensity of the echo to that of the original FID one can deduce the characteristic spin–spin relaxation time $T_2$. In PGSE NMR, however, one is not interested in $T_2$ but in the self-diffusion velocity of the studied molecules. Therefore, rather than correcting for magnetic field inhomogeneities an inhomogeneous field is created on purpose. This happens in a well-defined manner by applying a magnetic field gradient of strength $g$ along the sample tube, i.e. along the $z$-axis. Now different positions in the sample correspond to different Larmor frequencies which, in turn, are like spacial labels for the spins [64]. Consequently, if a molecule does not reside in the same position during the dephasing ($0 < t < \tau$) and the rephasing ($\tau < t < 2\tau$) period, which is the case when the molecule self-diffuses, the spin-echo signal is reduced. The observed echo attenuation is the stronger the bigger the gradient or the larger the molecule's displacement. The latter depends on the self-diffusion velocity, characterized by the self-diffusion coefficient $D$, as well as on the probed time span which in PGSE NMR experiments is conventionally called the 'diffusion time' $\Delta$. Concerning the magnetic field gradient it was found that pulsed rather than static gradients are more convenient [59] (actually this is where the name PGSE NMR comes from). Accordingly, the impact of the gradient depends both on the strength $g$ and the
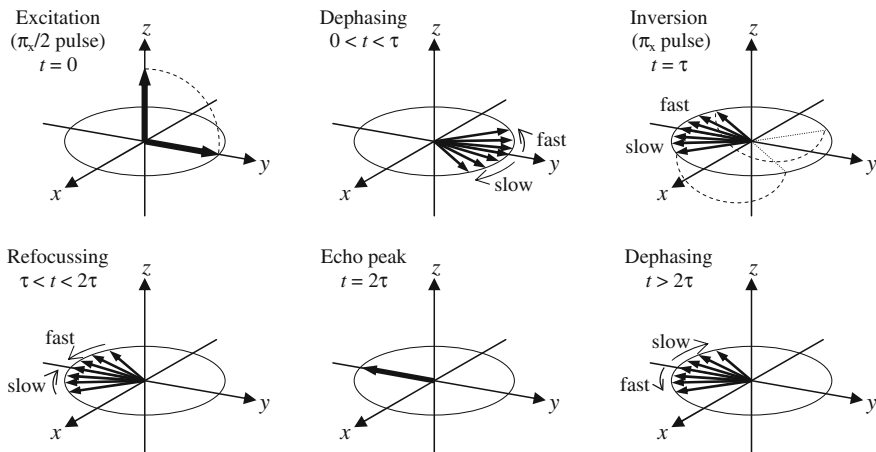
**Fig. 2.15** The $[\pi_x/2 - \tau - \pi_x - \tau]$ pulse sequence of the Hahn spin-echo experiment. (Reprinted from *Progress in NMR Spectroscopy*, Vol. 19, P. Stilbs, Fourier Transform Pulsed-Gradient Spin-Echo Studies of Molecular Diffusion, 1–45, Copyright 1987, with permission from Elsevier)

duration $\delta$ of these pulses. It holds for the influence of the parameters $D$, $\Delta$, $g$ and $\delta$ on the intensity $S$ of the echo signal at time $t = 2\tau$ [59]

$$S(2\tau) = S(0)\, e^{-2\tau/T_2}\, e^{-\gamma_g^2\, g^2\, D\delta^2\, (\Delta-\delta/3)} \tag{2.31}$$

where $S(0)$ is the FID intensity directly after the first $\pi_x/2$-pulse and $\gamma_g$ is the gyromagnetic ratio of the observed nucleus. The equation is specific for the so-called Stejskal Tanner PGSE NMR experiment [59], which is based on the Hahn spin-echo pulse sequence [63] explained above. Thus the first exponential term accounts for spin–spin relaxation with the transversal relaxation time $T_2$. The second exponential term, however, is determined exclusively by self-diffusion. If Eq. (2.31) is normalized with respect to the echo intensity observed in the absence of a magnetic field gradient, i.e.

$$S(2\tau)_{g=0} = S(0)\, e^{-2\tau/T_2}, \tag{2.32}$$

the universal Stejskal Tanner equation [59] for the echo signal attenuation $E$ due to self-diffusion in PGSE NMR experiments is obtained for which it holds

$$E = \frac{S(2\tau)}{S(2\tau)_{g=0}} = e^{-\gamma^2\, g^2\, D\delta^2(\Delta-\delta/3)}. \tag{2.33}$$

The Stejskal Tanner pulse sequence is depicted in Fig. 2.16 where the gradient strength $g$, the gradient duration $\delta$, the diffusion time $\Delta$ as well as the defocusing and the refocusing time periods $\tau$ are shown.
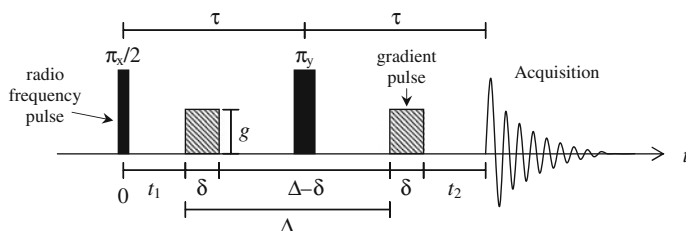
**Fig. 2.16** Pulse sequence of the Stejskal Tanner experiment (redrawn from [91] with permission of John Wiley and Sons)

When a molecule with the self-diffusion coefficient $D$ is studied in a Stejskal Tanner experiment with constant time period $\tau$, an increase of any of the parameters $g$, $\delta$ or $\Delta$ results in a stronger attenuation of the echo signal. Thus, if a series of measurements is performed in which one of these values is varied, $D$ can easily be obtained by fitting the experimental data to Eq. (2.33). In a semi-logarithmic plot of the echo attenuation $E$ versus the varied parameter or, respectively, versus the term $\left\{ \gamma_g^2 g^2 \delta^2 (\Delta - \delta/3) \right\}$, the self-diffusion coefficient $D$ can directly be extracted from the slope of the curve. Experimentally it is most convenient to change the gradient strength $g$ while keeping constant all times of the pulse sequence. Hence, the contribution of spin relaxation to the echo attenuation remains unaltered and simply cancels out. But also other practical issues have to be considered. For example, the diffusion time $\Delta$ as well as the gradient strength $g$ and duration $\delta$ must be chosen such that an echo signal with a reasonable signal-to-noise ratio is obtained. In this regard one must keep in mind that the echo attenuation in PGSE NMR experiments originates not only from self-diffusion but also from spin relaxation processes. In case of the standard $\left[ \pi_x/2 - \tau - \pi_y - \tau \right]$ Stejskal Tanner sequence (cp. Fig. 2.16), for example, it depends directly on the spin–spin relaxation time $T_2$. However, various sequences for specific situations have been developed (e.g. [65–67]). A well-established one is based on the stimulated spin-echo method by Hahn which comprises three $\pi_x/2$ radiofrequency pulses [63]. The corresponding PGSE NMR sequence with two additional magnetic field gradient pulses was first described by Tanner in 1970 [68] and is depicted in Fig. 2.17.

Tanner's stimulated echo sequence, just like the Stejskal Tanner experiment, comprises a first $\pi_x/2$-radiofrequency pulse which rotates the magnetisation in the $xy$-plane whereupon the spins start to dephase. Then, however, instead of a $\pi_x$-pulse a second $\pi_x/2$-pulse is applied which aligns the magnetisation again along the $z$-axis while the system memorizes the experienced loss of phase coherence. In this state the magnetisation is only subjected to spin–lattice relaxation which, as can be seen Fig. 2.17, holds true during most of the diffusion time $\Delta$. Hence, when longitudinal relaxation is slower than spin–spin relaxation, i.e. $T_1 \gg T_2$, which is true for many species, especially large molecules, the stimulated spin-echo method
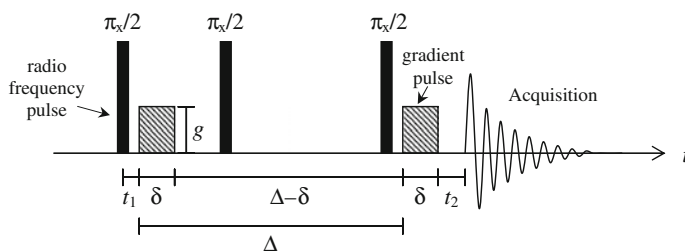
**Fig. 2.17** Pulse sequence of the Tanner pulsed-gradient stimulated spin-echo experiment (redrawn from [91] with permission of John Wiley and Sons)

by Tanner is often superior to the ordinary Stejskal Tanner experiment. As explained above, it allows under these circumstances to probe longer diffusion times $\Delta$, which gives the molecules enough time to move significant distances such that a measurable self-diffusion effect on the attenuation of the echo signal is obtained. The latter is finally stimulated by a third $\pi_x/2$ pulse which returns the magnetisation in the $xy$-plane restoring the spin's phase angles with reversed signs. One has to be aware that in this sequence the maximum amplitude of the stimulated echo detected after spin refocusing is intrinsically only 50 % of the original signal [68]. However, due to the explained advantages, the experiment is still often superior to other techniques and therefore frequently applied—just as in the work at hand. Further relevant experimental details like strategies to prevent convective flow in the sample due to temperature gradients and the application of magnetic field gradient pulses of non-rectangular shape are covered in the Experimental Methods (Sect. 6.7).

## 2.4.3 General Strategy for Studying Microemulsions via FT-PGSE NMR Spectroscopy

As mentioned above, the basic fact which allows studying the microstructure of microemulsions by PGSE NMR spectroscopy is that self-diffusion coefficients contain structural information about a sample if free self-diffusion in the latter is confined on a length scale probed in the experiment [64]. A detailed explanation of how this principle applies to microemulsions will be given below. Furthermore, the Fourier transform (FT) extension of the PGSE method opens up the possibility to simultaneously measure the self-diffusion coefficients $D$ of several components in one sample [69], e.g. water, the oil compound as well as the surfactant in a microemulsion.

A typical diffusion time applied in a PGSE NMR experiment is $\Delta = 10$ ms. Thus, according to Eq. (2.28), after this period the average one-dimensional displacement of an $H_2O$ molecule in a pure water sample with $D_{0,H_2O} = 2.3 \times 10^{-9}$ m$^2$ s$^{-1}$ at 25 °C [70] is 6.8 μm. (Note that due to the simple magnetic field gradient along the

$z$-axis only the self-diffusional motion in this single direction is monitored, i.e. $n = 2$ in Eq. (2.28)). A microemulsion, however, possesses a microstructure with domain sizes in the nanometer range. Hence, travelling over micrometer distances a water molecule in the microemulsion encounters obstruction which hinders its motion. In detail, what is observed is the following: In the case of a water-in-oil droplet microemulsion a water molecule reaches numerous times the confining surfactant layer at the water–oil interface during the investigated time span $\Delta$. Therefore, the effective displacement of the water molecule is just as big as the displacement of the droplet it resides in. Because the latter moves relatively slow, a quite small $D_{H_2O}$ value results. In a bicontinuous microemulsion the situation is different. Here the self-diffusion of the $H_2O$ molecule in the water domains is only restricted in two dimensions. Accordingly, one measures a larger self-diffusion coefficient $D_{H_2O}$ than in the water-in-oil droplet microemulsion. Eventually, when an oil-in-water droplet microemulsion is formed, $D_{H_2O}$ approaches the value $D_{0,H_2O}$ for unrestricted self-diffusion since water is the continuous phase of the system. The presence of the oil droplets gives rise to only minor obstructive effects determined by the droplet volume fraction and shape. This discussion demonstrates how measuring the self-diffusion coefficient of water one can monitor the change of the microstructure in a microemulsion [71–74]. Of course, exactly the same observations as for $D_{H_2O}$, albeit inversed, are made for the self-diffusion coefficient of the oil component $D_{oil}$. The surfactant molecules at the water–oil interface, by contrast, travel in both water-in-oil and oil-in-water microemulsions effectively just as fast as the microemulsion droplets. However, in bicontinuous microemulsions one observes lateral self-diffusion of the surfactant molecules along the interfacial layer and therefore in principle a maximum of $D_{surfactant}$ [73].

In this thesis microemulsions with non-ionic surfactants are studied which change their microstructure as a function of temperature. Hence, when this change is followed with the FT-PGSE NMR method it is important to keep in mind that self-diffusion is a temperature-dependent process itself. Originating in the thermal motion of the molecules, which increases with increasing temperature, the self-diffusion coefficients are naturally the bigger the higher temperature. This is directly found for $D_0$ of pure substances. The self-diffusion coefficients $D$ measured in structured systems, however, combine the temperature and the microstructure effects. In order to interpret the self-diffusion coefficients measured in a microemulsion in terms of the microstructure it is therefore advisable to normalize them with respect to the self-diffusion coefficients $D_0$ of the pure solvents [75]

$$D_{rel} = \frac{D}{D_0}. \tag{2.34}$$

If the relative self-diffusion coefficients of water and oil are then plotted versus the temperature, i.e. the tuning parameter for the microstructure, one finds the values changing as shown schematically in Fig. 2.18.

**Fig. 2.18** Schematic diagram of the normalized self-diffusion coefficients $D_{rel}$ of water and oil in a non-ionic microemulsion plotted versus the temperature $T$ [92]. For an ideal structure and equal volume fractions of water and oil the intersection of the two curves is located at $D_{rel} = 2/3$ [75] and $T = \widetilde{T}$
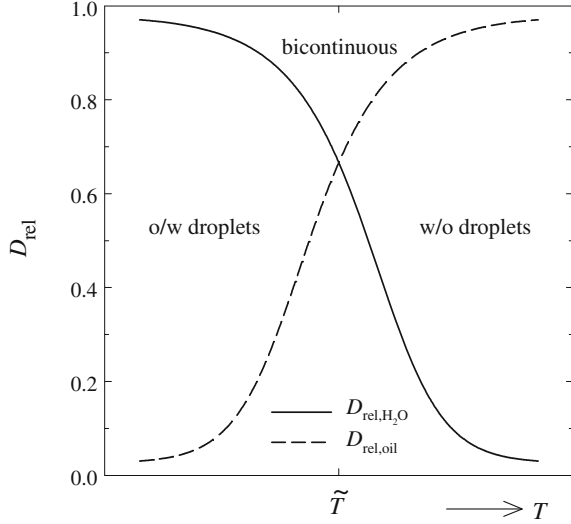
According to the explanation given above, the parameter $D_{rel}$, which is also referred to as "obstruction factor", is in droplet microemulsions high for the molecules of the continuous phase and small for the species enclosed in the droplets [73]. Thus, within the transition from a oil-in-water droplet microemulsion at low temperatures to a water-in-oil droplet microemulsion at high temperatures $D_{rel,H_2O}$ continuously decreases while $D_{rel,oil}$ continuously increases, respectively (see Fig. 2.18). In the intermediate bicontinuous regime where the microstructure inverts as the mean curvature of the surfactant layer runs through zero at $T = \widetilde{T}$ the relative self-diffusion coefficients of water and oil are equal. Hence $D_{rel,H_2O}(T)$ and $D_{rel,oil}(T)$ intersect for which it holds [75]

$$D_{rel,H_2O}\big(\widetilde{T}\big) = D_{rel,oil}\big(\widetilde{T}\big) = \frac{2}{3}, \qquad (2.35)$$

given that the volume ratio of water and oil in the microemulsion is 1:1 and the structure is without any defects.

## 2.5  Small Angle Neutron Scattering

Small angle neutron scattering (SANS) is a powerful method for studying the microstructure of soft matter materials in size ranges from a few Ångströms up to hundreds of nanometers [76]. The underlying basic scattering theory is the same as for other small angle scattering experiments like small angle X-ray scattering (SAXS) or small angle light scattering (SALS). In fact, while Guinier's pioneering

work on SAXS dates to the late 1930s [77] the development of SANS started about 30–40 years later [76, 78]. This is because only then suitable techniques for the generation of free neutrons and their detection became available. Free neutrons can only be generated in large-scale facilities such as the research reactor of the Institute Laue-Langevin (ILL) in Grenoble, France, or the Research Neutron Source Heinz Maier-Leibnitz (FRM II) in Garching near Munich, Germany. Therefore beam time for SANS experiments is usually limited. However, applying for beam time and spending nights in the neutron guide hall is well worth the effort because of the inherent advantages of the SANS method. First of all it is completely non-destructive, i.e. the neutron radiation does not alter the sample. Secondly, SANS offers the unique possibility to vary and adjust the scattering contrast by selectively deuterating different sample components [76, 78, 79]. This allows masking or, respectively, highlighting different parts of the microstructure.
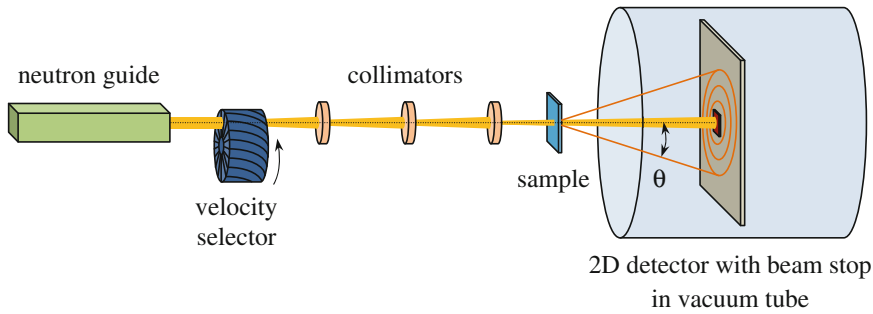
### 2.5.1 The SANS Experiment

When free neutrons are generated in a nuclear reactor in a controlled fission reaction of, e.g., uranium ($^{235}$U) this happens at extremely high temperatures which means that the free neutrons move very fast. Due to the thermal energy of the order of $k_B T$ a neutron has the velocity

$$v = \sqrt{\frac{2\,k_B\,T}{m_{neutron}}} \qquad (2.36)$$

in which $k_B$ is the Boltzmann constant, $T$ the absolute temperature and $m_{neutron} = 1.675 \times 10^{-27}$ kg [62] the mass of the particle. Moreover, one can ascribe a certain wavelength $\lambda$ to the moving neutron according to the de Broglie formalism. With the Planck constant $h$ one yields

$$\lambda = \frac{h}{v\,m_{neutron}}. \qquad (2.37)$$

The idea of the wave-particle duality is important for the SANS experiment because the scattering pattern is understood as the result of superimposed neutron waves, as will shortly be explained, while one records it by counting the number of neutrons encountering the detector plane [76]. However, before the generated neutrons are guided to the sample they are slowed down in a so-called moderator. The latter transforms the initially "hot" neutrons, moving with more than 4,000 m s$^{-1}$, to "thermal" and "cold" neutrons which are used for the SANS experiment [76]. Typically one works with neutron beams with wavelengths in the order of 10 Å which, according to Eqs. (2.36) and (2.37), corresponds to cold neutrons ($T \approx 10$ K) moving with a velocity of about 400 m s$^{-1}$. The moderated neutron beam is monochromized by a mechanical velocity selector, i.e. a rotating

**Fig. 2.19** Schematic representation of the set-up of a SANS experiment in which one detects the intensity of the scattered neutron beam at different scattering angles θ. (Redrawn and modified from http://physics.unifr.ch/en/page/296/, 09.07.2013)

cylinder with helically curved slits which, according to its rotation speed, lets pass only neutrons of a certain narrow velocity distribution of the order of $\Delta\lambda/\lambda \approx 10~\%$. This distribution can further be confined by a so-called chopper after which one adjusts the divergency and diameter of the neutron beam with a set of collimators. Finally, an aperture defines the beam size and shape directly in front of the sample. Since most of the neutrons pass the sample without deflection it is necessary to place a 'beam stop' in the center of the detector plane in order to prevent damage through the intense direct beam [78]. The sample-detector distance is variable because the detector plane can be moved back and forth in a big vacuum tube. A schematic representation with the most important elements of the instrumental set-up is shown in Fig. 2.19.
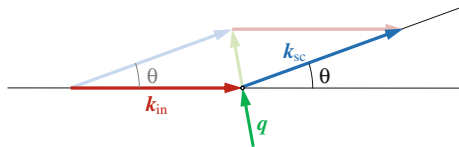
The dimensions of the detector unit directly determine which scattering angles are experimentally accessible. For example the instrument D11 at the ILL in Grenoble, which was used for this work, has a detector with an area of $96 \times 96~cm^2$ that can be moved to sample-detector distances from 1.2 to 39.0 m.[1] Thus, with a centered beam stop of $5 \times 5~cm^2$ one can detect scattering at angles between 21.80° and 0.04°. Together with the chosen wavelength of the neutron beam this defines which microstructure size range can be studied as will become obvious from the scattering theory.

## 2.5.2 Basic Scattering Theory

In the SANS experiment the distances from the neutron source to the sample and from the sample to the detector are much larger than the wavelength of the neutron

---

[1] http://www.ill.eu/instruments-support/instruments-groups/instruments/d11/characteristics/, 09.07.2013.

**Fig. 2.20** Illustration of the wave-vectors of an incident and an elastically scattered beam, $k_{\text{in}}$ and $k_{\text{sc}}$, respectively, and the momentum transfer vector $q$ which characterizes the scattering process in the scattering angle $\theta$

beam. Therefore one can work with the far field (or Fraunhofer) approximation which states that radiation which is emitted as spherical waves can at large distances be treated as possessing a planar wave front. This is thus true for both the incident neutron beam at the sample position and for the scattered radiation reaching the detector. Accordingly, the incident and the scattered neutrons are represented by wave-vectors, $k_{\text{in}}$ and $k_{\text{sc}}$, respectively, which point in the directions of the waves' propagation while their magnitude $k$ is defined by the wavelength $\lambda$

$$k = |\boldsymbol{k}| = \frac{2\pi}{\lambda}. \tag{2.38}$$

Since it is assumed that the scattering process in the SANS experiment is elastic the neutrons retain their energy and only change their direction when interacting with the sample. Therefore the incident and the scattered beam possess the same wavelength such that the magnitudes of $k_{\text{in}}$ and $k_{\text{sc}}$ are equal, i.e. $k_{\text{in}} = k_{\text{sc}}$. The change of the direction of propagation can be ascribed to a momentum transfer for which one defines the momentum transfer vector

$$\boldsymbol{q} \equiv \boldsymbol{k}_{\text{sc}} - \boldsymbol{k}_{\text{in}} \tag{2.39}$$

as illustrated in Fig. 2.20.

The $q$ vector, also often referred to as the 'scattering vector', and particularly its magnitude $q$ are very important in the scattering theory. For $q$ it holds according to geometrical considerations (cp. Fig. 2.20) and using Eq. (2.38)

$$q = |\boldsymbol{q}| = 2\,k\,\sin\frac{\theta}{2} = \frac{4\pi}{\lambda}\,\sin\frac{\theta}{2} \tag{2.40}$$

where $\theta$ is the scattering angle between the incident and the scattered beam, which both possess the wavelength $\lambda$ and wave-vectors of magnitude $k$. Following the examples given above, with a neutron beam of $\lambda = 10$ Å and scattering angles $\theta$ between $0.04°$ and $21.80°$ a $q$ range from $4.4 \times 10^{-4}$ to $2.4 \times 10^{-1}$ Å$^{-1}$ is covered. Through $\lambda$ variations this range can further be stretched. Note that in SANS experiments one usually quotes the space-resolved scattering intensity not as a function of the scattering angle $\theta$ but as a function of $q$ which allows, e.g., to combine data measured at different wavelengths.

Constructive interference of waves, which is a prerequisite for generating a signal on the detector, occurs, according to Bragg's law, only when the path difference of two rays deflected at two sites with distance $d$ is a multiple of their wavelength $\lambda$. Accordingly it holds for scattering at a scattering angle $\theta$

$$2\,d\,\sin\frac{\theta}{2} = n\,\lambda \tag{2.41}$$

where $n$ is an integer $\geq 1$ and $d$ the distance between two scattering centers in the sample. If the Eqs. (2.40) and (2.41) are combined one obtains (for $n = 1$) a fundamental relationship between $q$ and the length scale $d$ of the microstructure, namely

$$q = \frac{2\pi}{d}. \tag{2.42}$$

This allows to finally calculate that with a SANS experiment covering a typical $q$ range of, e.g., $4.4 \times 10^{-4}$ to $2.4 \times 10^{-1}$ $\text{Å}^{-1}$ one can probe a sample's microstructure on length scales between 1.4 μm and 2.6 nm, respectively.

### 2.5.3 Neutron Scattering

Neutrons are uncharged elementary particles with a spin of ½ and a magnetic moment of $\mu = -9.662 \times 10^{-27}$ J T$^{-1}$ [62]. Therefore, free neutrons which are irradiated on a sample interact with the atomic nuclei of the comprised atoms via the strong nuclear force [76]. Thereupon they can be scattered—if they are not adsorbed or directly transmitted, which actually happens to most of the neutrons. The likeliness for scattering depends on the type of the encountered atom and, remarkably, there are large differences for different isotopes (e.g. $^{1}$H and $^{2}$H) and for different spin-states. One can picture that the probability for scattering is the higher the bigger the surface of an atom 'seen' by the incident neutron. Thus one assigns to each atom $i$ a 'scattering cross-section'

$$\sigma_{\text{i}} = 4\pi\langle|b_{\text{i}}|\rangle^2 \tag{2.43}$$

where $b_{\text{i}}$ is the atom's 'scattering length' that characterizes its interaction range [78]. Note that each atom possesses a coherent as well as an incoherent scattering length. The respective incoherent scattering cross-section gives rise to an 'internal background', which the measured SANS data is corrected for [80]. Hence all further explanations will exclusively consider the coherent scattering.

With the atoms' scattering lengths $b_{\text{i}}$, which are tabulated for many nuclei, one can calculate the 'scattering length density' $\rho$ of the scattering microstructure units in the sample. The latter is an important parameter defining the amplitude of the

scattered neutron wave and thus the detected intensity. The scattering length density of, e.g., a molecule $k$ equals the sum of the scattering lengths $b_i$ of all comprised atoms $i$ divided by the volume of the molecule [78, 79]. This corresponds to

$$\rho_k = \frac{N_A\, \rho_k^0}{M_k} \sum_i b_i \tag{2.44}$$

where $N_A$ is the Avogadro constant, $M_k$ the molar mass of substance $k$ and $\rho_K^0$ its macroscopic density. In order to determine the scattering length density of a phase or a particle in which different components $k$ are mixed one can add up the individual scattering length densities $\rho_k$ weighted by the respective mole fractions $x_k$

$$\rho_{\text{mix}} = \sum_k (x_k\, \rho_k). \tag{2.45}$$

## 2.5.4 The Scattering Pattern

As mentioned previously, the detector in a SANS experiment counts how many neutrons arrive during the measuring time at different detector positions. SANS is therefore a static technique which averages out time-dependent fluctuations of the scattering signal. A scattering pattern is obtained which corresponds to the number of the scattered neutrons as a function of the scattering vector, $N(\boldsymbol{q})$. The number of detected neutrons depends on various parameters, namely (a) on the number of incident neutrons $N_{\text{in}}$, (b) on the fraction of neutrons which pass the sample without being absorbed, i.e. the sample's transmission $Tr$, (c) on the probability that an incident neutron encounters a scattering center which increases with the sample thickness $d_{\text{sample}}$, (d) on the size of the solid angle $\Omega$ within which scattering is detected, i.e. $\Delta\Omega$, and (e) last but not least on the density of the scatterers in the sample volume $V$ with the characteristic "scattering cross-sectional area ($\sigma$) per unit solid angle ($\Omega$)" [81] ($d\sigma/d\Omega$), usually referred to as 'differential scattering cross-section', [82]

$$N(\boldsymbol{q}) = N_{\text{in}} \cdot Tr \cdot d_{\text{sample}} \cdot \Delta\Omega \cdot \frac{1}{V} \frac{d\sigma(\boldsymbol{q})}{d\Omega}. \tag{2.46}$$

To evaluate the measured data one corrects for the experimental factors and considers exclusively the differential scattering cross-section per sample volume, denoted $(d\Sigma/d\Omega)$, which "represents the probability of a particle of the incident beam being scattered out from the unit sample volume into the solid angle $\Delta\Omega$" [80]. One also calls $(d\Sigma/d\Omega)$ the normalized 'scattering intensity' [78, 80, 82]

$$I(\boldsymbol{q}) = \frac{\mathrm{d}\Sigma(\boldsymbol{q})}{\mathrm{d}\Omega} = \frac{1}{V}\frac{\mathrm{d}\sigma(\boldsymbol{q})}{\mathrm{d}\Omega} = \frac{N(\boldsymbol{q})}{N_{\mathrm{in}}} \cdot \frac{1}{Tr \cdot d_{\mathrm{sample}} \cdot \Delta\Omega} \qquad (2.47)$$

the unit of which is an inverse length. With an isotropic distribution of scattering centers in the sample the detected scattering pattern can be radially averaged which reduces $I(\boldsymbol{q})$ to $I(q)$ [76, 78].

To understand the origin of the scattering intensity $I(\boldsymbol{q})$ it is expedient to regard the scattered neutrons as waves. They emerge from all scattering centers at the positions $\boldsymbol{r}$ in the scattering volume and interfere with each other when they are scattered in the same direction, i.e. with the same momentum transfer vector $\boldsymbol{q}$. The interference leads to a neutron wave 'seen' by the detector whose amplitude $A(\boldsymbol{q})$ is directly related to the detected intensity

$$I(\boldsymbol{q}) = A(\boldsymbol{q})\, A^*(\boldsymbol{q}) = |A(\boldsymbol{q})|^2. \qquad (2.48)$$

Assuming that all scattering events are independent (Born approximation) one can simply add the individual wave-functions of the scattered neutrons or rather integrate them over the whole scattering volume $V$. Accordingly, the amplitude of the detected neutron wave is [80, 82]

$$A(\boldsymbol{q}) = \int_V \rho(\boldsymbol{r})\, e^{-i\boldsymbol{q}\boldsymbol{r}}\, \mathrm{d}\boldsymbol{r} \qquad (2.49)$$

where $i$ is the imaginary unit and $\rho(\boldsymbol{r})$ the scattering length density at the position $\boldsymbol{r}$. The scattering length density can be expressed as 'fluctuating' in the sample volume by $\Delta\rho(\boldsymbol{r})$ around a mean value $\bar{\rho}$ [83]

$$\rho(\boldsymbol{r}) = \bar{\rho} + \Delta\rho(\boldsymbol{r}). \qquad (2.50)$$

Thus it can be shown that it is the fluctuations of the scattering length density which determine the detectable scattering intensity around the primary beam, i.e. $I(q)_{q>0}$, because it holds for the amplitudes of the neutrons which are not scattered in forward direction

$$A(\boldsymbol{q})_{q>0} = \int_V \Delta\rho(\boldsymbol{r})\, e^{-i\boldsymbol{q}\boldsymbol{r}}\, \mathrm{d}\boldsymbol{r}. \qquad (2.51)$$

In other words, a scattering pattern is only observed when in the studied sample zones of different scattering length densities $\rho$ are present on the probed length scale, which simply means the sample has a microstructure with a 'scattering contrast'

$$\Delta\rho = |\rho_{\mathrm{s}} - \rho_{\mathrm{m}}| \qquad (2.52)$$

where $\rho_{\mathrm{s}}$ is the scattering length density of the scatterer and $\rho_{\mathrm{m}}$ that of the surrounding matrix [76].

## 2.5.5 Solving the Scattering Problem

When the microstructure of a sample is known it is theoretically possible to compute the corresponding scattering intensity $I(q)$ by Fourier transforming its convoluted scattering length density profile which equals building the complex square of the scattered neutron waves amplitude (cp. Eq. 2.49). In principle one can also go the inverse way, Fourier transform the measured scattering intensity, deconvolute the result and estimate the system's microstructure [83]. However, since the SANS data is only measured in a limited $q$ range its Fourier transform often possesses strong termination effects. Moreover, the deconvolution is only feasible for discrete scattering particles with a simple geometry while it fails for complex systems like bicontinuous microemulsions. Hence it is often more convenient to presume a justified model for the microstructure, calculate the respective scattering function, compare it with the measured data and adjust the model if necessary. Sample characteristic parameters, like for example a particle diameter, are then yielded as the fit parameters.

If one wants to compute a system's scattering function $I(q)$ one must be aware of the different factors which contribute to the scattering intensity. This is in detail (a) the number density of the scatterers, (b) their individual shape and local scattering contrast as well as (c) their spatial correlation. Usually one distinguishes between the 'form factor' $P(q)$, which comprises the internal scattering contributions of discrete scatterers like suspended particles, and the 'structure factor' $S(q)$, which accounts for the scattering contributions due to interactions between different scatterers. In the most general case both contributions are related to each other. However, in a simplified approach these relations are neglected and the scattering intensity is calculated as product of three independent factors ('decoupling approximation') [84]

$$I(q) = n \cdot \overline{P(q)} \cdot S_{\text{eff}}(q). \tag{2.53}$$

In this equation $n$ is the number density of the scatterers, i.e. their number $N$ divided by the sample volume $V$, $\overline{P(q)}$ is the average form factor and $S_{\text{eff}}(q)$ the effective structure factor. The latter two factors will be further explained in the following.

The **average form factor** $\overline{P(q)}$ allows for the fact that the scattering particles in a sample are usually not monodisperse. Their characteristic dimension $X$ rather possesses a certain distribution around a mean value $X_0$. Thus the average form factor is calculated as [85]

$$\overline{P(q)} = \int\limits_0^\infty P(q,X) \cdot W(X,X_0) \, \mathrm{d}X \tag{2.54}$$

where $W(X, X_0)$ is the distribution function, e.g. for a Gaussian distribution, and $P(q, X)$ is the form factor of a single particle. Form factors have been described for many different particle geometries. In general the form factor of a particle $k$ is the complex square of the amplitude $A_k(\boldsymbol{q})$ of the wave which is scattered from the particle. i.e. [85]

$$P(q) = \left\langle A_k(\mathbf{q}) \, A_k^*(\mathbf{q}) \right\rangle = \left\langle |A_k(\mathbf{q})|^2 \right\rangle \tag{2.55}$$

where the brackets denote an average over all particle orientations in the sample. With this average one yields for the amplitude, instead of the three-dimensional Fourier transform in Eq. (2.51), the one-dimensional radial symmetrical form

$$A_k(q) = 4\pi \, \Delta\rho \int\limits_0^\infty f(r) \, r^2 \, \frac{\sin(qr)}{qr} \, dr. \tag{2.56}$$

Here $f(r)$ is the normalized radial scattering length density distribution of the scatterer $k$ with the scattering contrast $\Delta\rho$ (cp. Eq. 2.52) and the characteristic radial scattering contrast profile $\Delta\rho(r)$

$$f(r) = \frac{\Delta\rho(r)}{\Delta\rho}. \tag{2.57}$$

Hence, the form factor of a scatterer of a certain shape can be determined based on the respective $f(r)$ function, for which many examples are found in the literature (e.g. core–shell particles [86]).

The **effective structure factor** $S_{eff}(q)$ accounts for the interference of neutron waves which are scattered from different particles $k$ and $l$ and possess the amplitudes $A_k$ and $A_l$, respectively. It holds [87, 88]

$$S_{eff}(q) = \frac{1}{\overline{P(q)}} \sum_k \sum_l A_k \, A_l \, S_{kl}(q) \tag{2.58}$$

where $\overline{P(q)}$ is the average form factor and $S_{kl}(q)$ the partial structure factor describing the correlation between the respective particles. To simplify the calculation of the structure factor one can, for example, assume that correlation occurs exclusively between particles of the same species $k$. If one furthermore neglects the dependence on the intraparticle scattering contributions one can replace the effective structure factor by an 'averaged structure factor' [84]

$$S_{av}(q) = \sum_k x_k \, S_k(q) \tag{2.59}$$

where $x_k$ is the molar fraction of particle species $k$. Of course one must evaluate in the individual case which assumptions are reasonable. In general, $S(q)$ depends on the scatterers' interaction potential which is accounted for in the 'pair correlation function' [78]

$$g(r) = e^{-\frac{V(r)}{k_B T}} \tag{2.60}$$

where $k_B$ is the Boltzmann constant, $T$ the absolute temperature and $V(r)$ the mean field potential or the pair interaction potential for relatively dilute systems, respectively. Thus, given that the interactions in the sample are isotropic, one can write for the structure factor [78]

$$S(q) = 1 + 4\pi n \int_0^\infty (g(r) - 1) \, r^2 \, \frac{\sin(qr)}{qr} \, dr \tag{2.61}$$

where $n$ is the number density of scatterers. Note that the structure factor is particularly relevant in concentrated systems where the scatterers significantly interact with their neighbours such that the microstructure is locally ordered. In highly diluted systems $S(q)$ tends to unity [85].

# References

1. T. Sottmann, C. Stubenrauch, in *Microemulsions: Background, New Concepts, Applications, Perspectives*, ed. by C. Stubenrauch (Wiley, Oxford, 2009), pp. 1–83
2. T.P. Hoar, J.H. Schulman, Nature **152**, 102–103 (1943)
3. P.A. Winsor, *Solvent Properties of Amphiphilic Compounds* (Butterworths Sci. Pubs., London, 1954)
4. S.I. Ahmad, K. Shinoda, S. Friberg, J. Colloid Interface Sci. **47**, 32–37 (1974)
5. K. Shinoda, S. Friberg, Adv. Colloid Interface Sci. **4**, 281–300 (1975)
6. K. Shinoda, H. Kunieda, N. Obi, S.E. Friberg, J. Colloid Interface Sci. **80**, 304–305 (1981)
7. M. Kahlweit, J. Colloid Interface Sci. **90**, 197–202 (1982)
8. M. Kahlweit, E. Lessner, R. Strey, J. Phys. Chem. **87**, 5032–5040 (1983)
9. M. Kahlweit, E. Lessner, R. Strey, J. Phys. Chem. **88**, 1937–1944 (1984)
10. M. Kahlweit, R. Strey, Angew. Chem. **97**, 655–669 (1985)
11. K. Shinoda, M. Araki, A. Sadaghiani, A. Khan, B. Lindman, J. Phys. Chem. **95**, 989–993 (1991)
12. M. Laupheimer, S. Engelskirchen, K. Tauber, W. Kroutil, C. Stubenrauch, Tenside Surf. Det. **48**, 28–33 (2011)
13. R. Tessendorf, *Microemulsions as Templates for High Surface Area Polymers* (WiKu-Wissenschaftsverlag Dr. Stein, Köln, 2009)
14. H.D. Dörfler, A. Grosse, Prog. Colloid Polym. Sci. **101**, 113–115 (1996)
15. M.J. Lawrence, G.D. Rees, Adv. Drug Deliv. Rev. **45**, 89–121 (2000)
16. A. Lattes, I. Rico, Surf. Sci. Ser. **24**, 377–385 (1987)
17. H. Gao, J. Li, B. Han, W. Chen, J. Zhang, R. Zhang, D. Yan, Phys. Chem. Chem. Phys. **6**, 2914–2916 (2004)

18. R.F. Joubran, D.G. Cornell, N. Parris, Colloid Surf. A **80**, 153–160 (1993)
19. C.T. Lee Jr., W. Ryoo, P.G. Smith Jr., J. Arellano, D.R. Mitchell, R.J. Lagow, S.E. Webber, K.P. Johnston, J. Am. Chem. Soc. **125**, 3181–3189 (2003)
20. A.F. Forziati, J. Res. Nat. Bur. Stand. **36**, 129–136 (1946)
21. S. Burauer, T. Sachert, T. Sottmann, R. Strey, Phys. Chem. Chem. Phys. **1**, 4299–4306 (1999)
22. M. Kahlweit, R. Strey, D. Haase, P. Firman, Langmuir **4**, 785–790 (1988)
23. R. Strey, Colloid Polym. Sci. **272**, 1005–1019 (1994)
24. W. Helfrich, Z. Naturforsch. C **28**, 693–703 (1973)
25. T. Sottmann, R. Strey, J. Chem. Phys. **106**, 8606–8615 (1997)
26. L. Salomonsson, G. Stang, B. Zhmud, Tribol. Trans. **50**, 302–309 (2007)
27. P. Terech, Colloid Polym. Sci. **269**, 490–500 (1991)
28. P. Terech, R.G. Weiss, Chem. Rev. **97**, 3133–3159 (1997)
29. M. George, R. G. Weiss, in *Molecular Gels: Materials with Self-Assembled Fibrillar Networks*, ed. by R.G. Weiss, P. Terech (Springer, Dordrecht, 2006), pp. 449–551
30. G. Zhu, J.S. Dordick, Chem. Mat. **18**, 5988–5995 (2006)
31. R. G. Weiss, P. Térech, in *Molecular Gels. Materials with Self-Assembled Fibrillar Networks*, ed. by R.G. Weiss, P. Terech (Springer, Dordrecht, 2006), pp. 1–13
32. K. Nishinari, Progr.Colloid Polym. Sci. **136**, 87–94 (2009)
33. S.R. Raghavan, B.H. Cipriano, in *Molecular Gels. Materials with Self-Assembled Fibrillar Networks*, ed. by R.G. Weiss, P. Terech (Springer, Dordrecht, 2006), pp. 241–252
34. P. Terech, D. Pasquier, V. Bordas, C. Rossat, Langmuir **16**, 4485–4494 (2000)
35. J.P. Gong, in *Kobunshi Jiten (Dictionary of Polymer Science)*, ed. by A. Shoten (Society of Polymer Science, Tokyo, 2005) (in Japanese—literally cited in English in [Nis09])
36. P. H. Hermans, in *Colloid Science, Volume II: Reversible Systems*, ed. by H.R. Kruyt (Elsevier, Amsterdam, 1949), pp. 483–651
37. P. Terech, I. Furman, R.G. Weiss, J. Phys. Chem. **99**, 9558–9566 (1995)
38. P. Terech, V. Rodriguez, J.D. Barnes, G.B. McKenna, Langmuir **10**, 3406–3418 (1994)
39. M.A. Rogers, T. Pedersen, L. Quaroni, Cryst. Growth Des. **9**, 3621–3625 (2009)
40. R. Wang, X.-Y. Liu, J. Xiong, J. Li, J. Phys. Chem. B **110**, 7275–7280 (2006)
41. P. Terech, Progr. Colloid Polym. Sci. **102**, 64–70 (1996)
42. M.A. Rogers, A.G. Maragoni, Langmuir **25**, 8556–8566 (2009)
43. M. Burkhardt, S. Kinzel, M. Gradzielski, J. Colloid Interface Sci. **331**, 514–521 (2009)
44. R. Lam, L. Quaroni, T. Pederson, M.A. Rogers, Sof Matter **6**, 404–408 (2010)
45. M.A. Rogers, A.G. Marangoni, Cryst. Growth Des. **8**, 4596–4601 (2008)
46. E. Ostuni, P. Kamaras, R.G. Weiss, Angew. Chem. Int. Ed. **35**, 1324–1326 (1996)
47. K.A. Dawson, Curr. Opin. Colloid Interface Sci. **7**, 218–227 (2002)
48. D. Jordan Lloyd, in *Colloid Chemistry,* vol. 1, ed. by J. Alexander (The Chemical Catalog Co., New York, 1926), pp. 767–782
49. K. Almdal, J. Dyre, S. Hvidt, O. Kramer, Macromol. Chem. Macromol. Symp. **76**, 49–51 (1993)
50. G. Böhme, *Strömungsmechanik nicht-newtonscher Fluide* (Teubner, Stuttgart, 1981)
51. R. Brummer, *Rheology Essentials of Cosmetic and Food Emulsions* (Springer, Berlin, 2006)
52. J.W. Goodwin, R.W. Hughes, *Rheology for Chemists: An Introduction*, 2nd edn. (RCS Publishing, Cambridge, 2008)
53. M.A. Rao, *Rheology of Fluid and Semisolid Foods: Principles and Applications* 2nd edn, ed. by G.V. Barbosa-Cánovas (Springer, New York, 2007)
54. T.F. Tadros, *Rheology of Dispersions: Principles and Applications* (Wiley-VCH, Weinheim, 2010)
55. R.I. Tanner, *Engineering Rheology*, 2nd edn. (Oxford University Press, New York, 2000)
56. R. Edgeworth, B. J. Dalton, T. Parnell, Eur. J. Phys. **5**, 198–200 (1984)
57. Homepage of University of Queensland, http://smp.uq.edu.au/content/pitch-drop-experiment. Accessed 03 May 2013
58. http://en.wikipedia.org/wiki/Pitch_drop_experiment. Accessed 03 May 2013
59. E.O. Stejskal, J.E. Tanner, J. Chem. Phys. **42**, 288–292 (1965)

60. E. Hawlicka, Chem. Soc. Rev. **24**, 367–377 (1995)
61. J. Crank, *The Mathematics of Diffusion* (Oxford University Press, Oxford, 1975)
62. P.W. Atkins, *Physikalische Chemie—Dritte, korrigierte* (Wiley-VCH, Weinheim, 2002)
63. E.L. Hahn, Phys. Rev. **80**, 580–594 (1950)
64. W.S. Price, Concepts Magn. Reson. **9**, 299–336 (1997)
65. R.M. Cotts, M.J.R. Hoch, T. Sun, J.T. Markert, J. Magn. Reson. **83**, 252–266 (1989)
66. W. Heink, J. Kärger, H. Pfeifer, J. Chem. Soc. Chem. Commun. **20**, 1454–1455 (1990)
67. T. Saito, P.L. Rinaldi, J. Magn. Reson. **130**, 135–139 (1998)
68. J.E. Tanner, J. Chem. Phys. **52**, 2523–2526 (1970)
69. P. Stilbs, Prog. Nucl. Magn. Reson. Spectrosc. **19**, 1–45 (1987)
70. R. Mills, J. Phys. Chem. **77**, 685–688 (1973)
71. M.T. Clarkson, D. Beaglehole, P.T. Callaghan, Phys. Rev. Lett. **54**, 1722–1724 (1985)
72. B. Lindman, P. Stilbs, M.E. Moseley, J. Colloid Interface Sci. **83**, 569–582 (1981)
73. B. Lindman, U. Olsson, Ber. Bunsenges. Phys. Chem. **100**, 344–363 (1996)
74. P. Stilbs, M.E. Moseley, B. Lindman, J. Magn. Reson. **40**, 401–404 (1980)
75. D.M. Anderson, H. Wennerström, J. Phys. Chem. **94**, 8683–8694 (1990)
76. M. Engel, T. Spehr, B. Stühn, Bunsen-Magazin **1**, 4–15 (2011)
77. A. Guinier, Ann. Phys. Paris. **12**, 161–237 (1939)
78. I. Grillo, in *Soft Matter Characterization*, ed. by R. Borsali, R. Pecora (Springer, New-York, 2008), pp. 723–782
79. P. Schurtenberger, in *Neutrons, X-rays and Light: Scattering Methods Applied to Soft Condensed Matter*, ed. by P. Lindner, T. Zemb (Elsevier, Amsterdam, 2002), pp. 145–170
80. P. Lindner, in *Neutrons, X-rays and Light: Scattering Methods Applied to Soft Condensed Matter*, ed. by P. Lindner, T. Zemb (Elsevier, Amsterdam, 2002), pp. 23–48
81. P. N. Pusey, in *Neutrons, X-rays and Light: Scattering Methods Applied to Soft Condensed Matter*, ed. by P. Lindner, T. Zemb (Elsevier, Amsterdam, 2002), pp. 3–21
82. O. Spalla, in *Neutrons, X-rays and Light: Scattering Methods Applied to Soft Condensed Matter*, ed. by P. Lindner, T. Zemb (Elsevier, Amsterdam, 2002), pp. 49–71
83. O. Glatter, in *Neutrons, X-rays and Light: Scattering Methods Applied to Soft Condensed Matter*, ed. by P. Lindner, T. Zemb (Elsevier, Amsterdam, 2002), pp. 73–102
84. B. Weyerich, J. Brunner-Popela, O. Glatter, J. Appl. Cryst. **32**, 197–209 (1999)
85. M. Kotlarchyk, S.-H. Chen, J. Chem. Phys. **79**, 2461–2469 (1983)
86. T. Foster, J. Phys. Chem. B **115**, 10207–10217 (2011)
87. P.N. Pusey, H.M. Fijnaut, A. Vrij, J. Chem. Phys. **77**, 4270–4281 (1982)
88. P. Salgi, R. Rajagopalan, Adv. Colloid Interface Sci. **43**, 169–288 (1993)
89. T. Sottmann, R. Strey, Ber. Bunsenges. Phys. Chem. **100**, 237–241 (1996)
90. O. Holderer, N.R. de Souza, M. Monkenbusch, *The Jülich Neutron Spin-Echo Spectrometer J-NSE* (poster), http://www.jcns.info/src/POFposters/JCNS_Poster_JNSE_science_v1.pdf. Accessed 10 March 2010
91. W.S. Price, Concepts Magn. Reson. **10**, 197–237 (1998)
92. C. Stubenrauch, *Mikroemulsionen mit Alkylgucosiden aus makroskopischer und NMR-spektroskopischer Sicht* (Shaker Verlag, Aachen, 1997)

Gelled Bicontinuous Microemulsions
A New Type of Orthogonal Self-Assembled Systems
Laupheimer, M.
2014, XXI, 161 p. 81 illus., 35 illus. in color., Hardcover
ISBN: 978-3-319-07718-5